Dynamics of core-mantle separation:

Influence of viscosity contrast and metal/silicate partition coefficients on the chemical equilibrium

V. Clesi[a,*], J. Monteux[a], B. Qaddah[a,b], M. Le Bars[b], J.-B. Wacheul[b], M.A. Bouhifd[a]

[a]Université Clermont Auvergne, CNRS, IRD, OPGC, Laboratoire Magmas et Volcans, F-63000 Clermont-Ferrand, France

[b]CNRS, Aix Marseille Université, Centrale Marseille, Institut de Recherche sur les Phénomènes Hors Equilibre, UMR 7342, 49, Rue F. Joliot-Curie - B.P. 146, 13384 Marseille Cedex 13, France

*Corresponding author: vincent.clesi@univ-lyon1.fr

Present address: Laboratoire de Géologie de Lyon- Terre, Planètes, Environnement, CNRS UMR 5276, ENS de Lyon, Université Lyon 1. Campus de la Douà, Batiment Geode, 2 Rue Raphaël Dubois, 69622 Villeurbanne Cedex.

Abstract

The composition of the Earth's core and mantle is set by the chemical equilibrium between metals and silicates during core/mantle segregation. The metallic core separated from the mantle by gravitational descent in the form of diapirs in a magma ocean, and therefore the dynamics of the diapir's downward movement has an influence on the chemical equilibrium. In this study, we characterize the descent of metallic droplets into a molten silicate using numerical models. By varying the silicate and metal viscosities (between 0.1 and 1000 Pa.s for each phase) as well as the partition coefficient between metal and silicate ($D^{met/sil}$, varying between 1 and 1000), we obtained quantifying parametrizing equations for the degree of equilibrium between molten metal and molten silicate, in a regime characterized by low *We* (*We* < 10) and low *Re* (10^{-3}<*Re*<10^{2}). We showed that the main parameters controlling the equilibrium for a siderophile element are the viscosity of the silicate and the partition coefficient. We applied our parameterization for Ni and Co in the context of late accretion on Earth so as to quantify the variation of the Ni/Co ratio after a large impact as a function of the magma ocean viscosity, for an iron-rain scenario of metal/silicate segregation. Using previous models (Canup, 2004) of the Moon–forming impact, we showed that the Moon formation had an effect on the current Ni/Co ratio. Depending on the radius of Theia's core and the viscosity of the magma ocean produced after the impact between the proto-Earth and Theia, the Moon formation could account for 0.45 % to 3 % of the current Ni/Co ratio for magma ocean viscosities of 0.1 to 100 Pa.s, respectively.

1. Introduction

The main process occurring on Earth during the first 100-150 million years was the segregation of its metallic Fe-rich core (*e.g.* Bouhifd et al., 2017; Rubie et al., 2015; Wood et al., 2006; and references therein). One major consequence of this segregation is the depletion of the Earth's mantle in the siderophile elements relative to primitive solar system abundances (*e.g.* Jones and Drake, 1986).

The most recent Earth core formation models include a combination of multistage core-mantle differentiation with N-body accretion simulations, combined with continuous Earth core formation where pressure, temperature, oxygen fugacity and chemical composition of both the mantle and core vary during accretion of the Earth (*e.g.* Rubie et al., 2015, and references therein). These models consider that the accretion of the Earth occurred during a series of large impact events (*e.g.* Canup, 2008; Wetherill, 1985; O'Brien et al., 2006; Monteux et al., 2009; Nakajima and Stevenson, 2015). More importantly, these models provide results for the metal-silicate partitioning of a significant number of siderophile elements, which are consistent with observed mantle abundances given that the oxygen fugacity increases from about IW-5 to IW-2 (5 to 2 log units lower than the Iron-Wüstite buffer) during core segregation (*e.g.* Cartier et al., 2014; Rubie et al., 2015; Wade and Wood, 2005).

In this context, the behavior of Ni and Co (two refractory and moderately siderophile elements) has been considered to provide an important indication of the conditions of

Earth core formation. The consensus is now that metal-silicate equilibration at high pressure, in the range of 40 – 60 GPa (corresponding to depths of 1000 – 1500 km), was required to produce the observed Ni and Co depletions in the mantle (Bouhifd and Jephcoat, 2011; Siebert et al., 2012; Righter, 2011; Fischer et al., 2015; Clesi et al., 2016, for some of the most recent studies). Similar conclusions were reached based on the metal-silicate partitioning of lithophile and weakly-siderophile elements (*e.g*. Mann et al., 2009). One can note here that the conditions of Earth core formation as derived from metal-silicate partitioning of several elements cannot be used as an argument for single-stage core formation. This is highly unlikely given that Earth core formation occurred over a series of large impact events.

Most core formation models are based on metal-silicate partitioning experiments where both phases are fully molten and both thermodynamic and kinetic equilibrium are reached. This type of scenario favors rapid core - mantle segregation, which is confirmed by isotopic studies on Hf/W and short lived isotopes (Kleine et al., 2002; Jacobsen et al., 2008). If the kinetic equilibrium is well constrained, the extent to which the mantle and core equilibrate with each other is model dependent. So we know that if the metal were to segregate by forming large diapirs descending through the silicate magma ocean, the timescale for the equilibration would be too long to explain the isotopic ratios of Hf/W (Rubie et al., 2003). Therefore, the metal could have segregated by forming smaller diapirs, or droplets, whose radius varied between 0.1 to 10 cm, forming a cloud of iron in

80 the magma ocean (Deguen et al., 2014; Wacheul et al., 2014). An intermediate scenario
81 combining iron-rain mingling for the first part of segregation in the magma ocean,
82 followed by creation of large descending diapirs also exists, which can explain the
83 equilibrium in a deep magma ocean. In such a scenario, the metal falls through the molten
84 silicate in the form of droplets, and then forms a metallic pond at the base of the magma
85 ocean. Gravitational instability then allows metal to form large diapirs which descend
86 through the solid layer of the mantle into the proto-core (*e.g.* Stevenson, 1981, Monteux
87 et al., 2015, Fleck et al., 2018). This study focuses on the iron-rain phase of core-mantle
88 segregation, during which chemical equilibrium is reached (Rubie et al., 2003, 2011), as
89 large diapirs have less chemical interaction with the surrounding fluid (Ulvrova et al.,
90 2011; Wacheul et al., 2014). In the scenario of segregation by iron rain (Fig. 1), the extent
91 to which the magma ocean is in equilibrium with the core depends on the properties of the
92 metallic flow. The physics of the fluid flow is dependent on various parameters, one of the
93 most important being the viscosity of the surrounding fluid (Ke and Solomatov, 2009;
94 Monteux et al., 2009; Ricard et al., 2009). Numerical and analog simulations of a metallic
95 diapir descending through a surrounding fluid with different viscosities have shown that
96 the diapir is more stable when surrounding viscosity increases from low values ($\sim 10^{-1}$
97 Pa.s) to high values ($\sim$ 100 Pa.s), (Samuel, 2012; Wacheul et al., 2014). This has an impact
98 on chemical equilibrium, since break–up of the diapir increases the surface of exchange
99 between metal and silicate and small droplets sink more slowly than large diapirs (Ulvrova

et al., 2011; Wacheul et al., 2014). The efficiency of equilibrium is also increased when internal convection favors homogenization of concentrations in the metallic droplets (Ulvrova et al., 2011).

The goal of the present study is to characterize the influence of viscosity (metal and silicate phases) and chemical equilibrium on the global equilibrium rate in a magma ocean. To do that, the most relevant methods are analog and numerical modeling (e.g. Samuel and Tackley, 2008; Sramek et al., 2010; Deguen et al., 2011; Wacheul et al., 2014). Numerical simulations are more practical than analog ones for studying the effects of different phenomena happening simultaneously. In addition, it is difficult to find analogs for both metal and silicate which will react exactly like these two phases, and even more complicated to find analogs that behave chemically and physically in the same way as molten metal and molten silicate. Given the limitations of analog experiments for multiple physical modeling, we chose to perform numerical simulations of a falling metallic sphere into a molten silicate using COMSOL Multiphysics 5.0 modeling software. This approach allows the chemical equilibrium for different types of siderophile elements to be determined. In our simulations we combined chemical diffusion calculations with different types of flow. In particular, these simulations led us to explore the contamination of a silicate column by an excess of a siderophile element initially present in the diapir. Since viscosity influences the type of flow, which in turn is crucial in core-mantle equilibrium modeling (Rubie et al., 2003; 2011; Samuel, 2012), viscosity must have an influence on

120 the extent of core-mantle equilibrium. Furthermore, the equilibrium depends on the
121 partition coefficients of the elements between metal and silicate ($D^{met/sil}$), which depend
122 on pressure, temperature, oxygen fugacity and composition of metal and silicate.
123 Therefore, we tested the contamination of silicate by generic siderophile elements using
124 four different values of $D^{met/sil}$ (1, 10, 100, 1000).

125 Since major chemical transfers likely occurred during the iron rain process (Rubie et
126 al., 2003) our simulations looked at the equilibrium of droplets with the surrounding
127 silicate. In general, large diapirs in a turbulent environment tend to break into small
128 droplets, forming a cloud in which each droplet moves at the same speed (Wacheul and
129 Le Bars, 2017, 2018). In this study, we look at how one droplet of a given radius (R_{Fe} = 1
130 cm), which can be deformed but cannot break (see Wacheul et al., 2014), interacts with
131 the surrounding silicate. Then this behavior is extrapolated to the entire droplet cloud, and
132 we can estimate the extent to which equilibrium is reached between the magma ocean and
133 the falling metal during planetary accretion.

134 As a result of these simulations, we constrain the chemical exchanges between a small
135 metallic diapir and a silicate volume as a function of silicate viscosity (varying from 0.1
136 Pa.s to 1000 Pa.s), the viscosity ratio between metal and silicate, and time. We thus
137 parameterize the effect of varying viscosity on metal-silicate equilibration, and we use this
138 parameterization to re-evaluate models of core-mantle segregation. Moreover, we
139 characterize the effect of changing the magma ocean viscosity on the chemical

composition of the mantle. Finally, we discuss the potential consequences of giant impacts such as the Moon-forming impact on the chemical composition of the Earth's mantle.

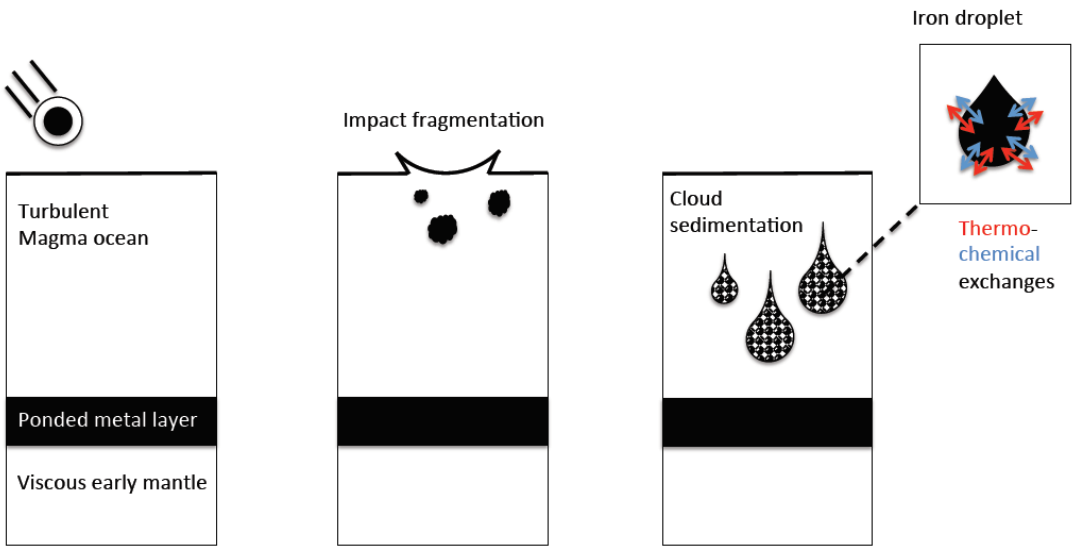

Figure 1: Schematics of core-mantle segregation. First, the impactor (metal+silicate) enters a turbulent magma ocean. The impactor is fragmented and melted on impacting the surface of the proto-planet. The metallic phase then forms a diapir which, if the magma ocean is turbulent enough, fragments into a cloud of droplets ranging in size from a few millimeters to 10 cm maximum (Rubie et al., 2011; Deguen et al, 2014; Wacheul et al., 2014; Wacheul and Le Bars, 2017,2018). Each droplet interacts with the surrounding silicate, exchanging heat and chemical elements, until it reaches thermo-chemical equilibrium with its environment.

155 **Table 1**

Parameter	Name	Values in this study
	All models	
ρ	Density of the fluid	silicate: 3300 - metal: 8000 kg.m^{-3}
t	Time	0.6 - 125 s
u	Velocity vector	m.s^{-1}
R_{Fe}	Radius of the diapir	1 cm
h_{max}	Maximum unit cell size	**0.1** × R_{Fe}
	Two-phase flow	
P	**Dynamic** Pressure of the fluid	1 atm
μ	Dynamic viscosity of the fluid	10^{-1} – 10^{3} Pa.s
g	Acceleration of gravity	9.81 m.s^{-2}
l	Distance fluid - initial interface	m
F_{st}	Surface tension force	Calculated for σ = 1 N.m^{-1}, in N.m^{-3}
Φ	Volume fraction of the fluid	**silicate: Φ =0 metal: Φ = 1 no unit**
ϵ_{ls}	**Parameter controlling interface reinitialization**	$h_{max}/2$

γ	**Parameter controlling velocity reinitialization**	**0.001 – 0.3 m.s^{-1}**
Transport of Diluted Species		
c_i	Concentration of element i	mol.m^{-3}
k_c	Diffusion coefficient of element i	10^{-6} m^2.s^{-1}
R_i	Reaction rate for element i	mol.m^{-3}.s^{-1}
N_i	Molar flux of element i	0 mol.m^{-2}.s^{-1}
Scaling of the study		
Re	Reynolds number	2.5×10^{-5} to 110
We	Weber number	2.3×10^{-5} to 3.5
R_μ	Viscosity ratio ($= \mu_{met}/\mu_{sil}$)	10^{-4} to 10^4
R_C	Ratio of the silicate volume reacted	see Section 3

Table 1: Parameters and variables used in this study. When values are not given, the variable is calculated later in the text (according to the specific case).

2. Physical Model

To model the sinking of a metallic droplet into a silicate liquid, we used the software COMSOL Multiphysics, and in particular the modules "Computational Fluids Dynamics" and "Chemical Reaction Engineering". In each module, a set of equations is defined and solved at each time step. These equations are described in the following subsections. The parameters we used for these equations are listed in Table 1.

2.1. Two-phase flow model

In our study, the fluid dynamics are governed by the Navier-Stokes equations that characterize:

- Conservation of mass

$$\nabla \cdot \boldsymbol{u} = 0 \tag{1}$$

- Conservation of momentum

$$\rho \frac{\partial \boldsymbol{u}}{\partial t} + \rho(\boldsymbol{u} \cdot \nabla)\boldsymbol{u} = -\nabla P\boldsymbol{I} + \nabla \cdot [\mu(\nabla \boldsymbol{u} + (\nabla \boldsymbol{u})^T)] + \rho \boldsymbol{g} + \boldsymbol{F_{st}} \tag{2}$$

Equation 1 is the conservation of mass for an incompressible fluid with $\boldsymbol{u}$ the flow velocity vector. Equation 2 describes the conservation of momentum, with acceleration of

the fluid ($\frac{\partial \boldsymbol{u}}{\partial t}$) and an inertia term ($\rho(\boldsymbol{u} \cdot \nabla)\boldsymbol{u}$) where ρ is fluid density. The first term on the right-hand side of Eq. 2 ($-\nabla P$) is the effect of the dynamic pressure P on the fluid. The second term ($\nabla \cdot [\mu(\nabla \boldsymbol{u} + (\nabla \boldsymbol{u})^T)]$) is the component representing the effect of viscous forces on the fluid with μ the fluid viscosity. The third term ($\rho \boldsymbol{g}$) is the gravitational force that applies to the whole domain with $\boldsymbol{g}$ the gravitational acceleration vector. The fourth term $\boldsymbol{F_{st}} = \nabla \cdot (\sigma(\boldsymbol{I} - \boldsymbol{n}\boldsymbol{n}^T)\delta)$ is the surface tension force with σ the surface tension coefficient, **I** the identity matrix, $\boldsymbol{n}$ a unit vector normal to the surface of interest and δ a smeared out Dirac function located at the interface. Since the volume of metal is small, we ignored the Coriolis forces in Eq. 2.

We monitored the interface between the liquid iron droplet and the molten silicates using the Level Set method, a Eulerian and implicit method used in multiphase flow problems (e.g. Qaddah et al., 2019). For that, we defined a function Φ, characterizing the silicate when Φ = 0 and the metal when Φ = 1. The boundary between the two phases was then set at Φ = 0.5. These values were obtained by modifying the level set field using a smeared out Heaviside function (Olsson & Kreiss, 2005), which allows direct calculation of the volume fraction of a given phase by integration of the variable Φ on the volume considered. The equation governing the transport of Φ is:

$$\frac{\partial \Phi}{\partial t} + \boldsymbol{u} \cdot \nabla \Phi = \gamma \nabla \left(\epsilon_{ls} \nabla \Phi - \Phi(1 - \Phi) \frac{\nabla \Phi}{|\nabla \Phi|} \right) \quad (3)$$

198 with γ (m/s) and ϵ_{ls} (m) the reinitialization parameters. The γ parameter limits the
199 numerical diffusion of the metallic phase during the simulation and needs to be adjusted
200 empirically when the viscosity varies. Indeed, γ is a parameter that determines the amount
201 of reinitialization or stabilization and must be carefully adjusted for each specific problem.
202 If γ is too low, the thickness of the interface might not remain constant, and oscillations in
203 Φ could appear because of numerical instabilities. On the other hand, if γ is too high, the
204 interface moves incorrectly. The ideal value of γ was given by the maximum velocity
205 reached by the diapir during its descent, as detailed in section 3. The range of values for γ
206 is given in Table 1. ϵ_{ls} is the parameter controlling the width of the interface between
207 fluids during reinitialization. This equation (Eq. 3) is a combination of the equations
208 presented in Olsson & Kreiss (2005), modified for the COMSOL in-built solver. This
209 solver allows the advection (on the left-hand side of the equation) and the reinitialization
210 parameter (right-hand side of the equation) to be solved at the same time. The dynamic
211 viscosity and the density are evaluated using the level set function and are defined by $\mu =$
212 $\mu_{sil} + \Phi(\mu_{met} - \mu_{sil})$ and $\rho = \rho_{sil} + \Phi(\rho_{met} - \rho_{sil})$, respectively (subscript *met* refers
213 to metal and *sil* to silicates). The resolution of the level set equation without using the
214 COMSOL Multiphysics module is detailed in Olsson & Kreiss, 2005. Furthermore, this
215 method has been already validated and applied to a similar problem in Qaddah et al., 2019.
216

The temperature of both the metallic droplets and the surrounding molten silicates is difficult to constrain. It is related to the history of both phases before the merging and involves radioactive heating, viscous dissipation and accretionary heating. In our study we consider that the impact that precedes the iron droplet sinking homogenizes the temperature of both phases. Hence, we do not consider heat conservation in the equations solved in our models, and focus instead on the chemical equilibration processes alone.

2.2. *Chemical model*

The chemical diffusion and reactions of elements are described by transport equations including an advective term to account for the movement of the phase and conservation of mass, a diffusion term (Fick's law) to account for diffusive transfer, and a reaction term to account for the chemical transfer based on the partition coefficient between metal and silicate. In our models we solve the following equation:

$$\frac{\partial c_i}{dt} + \nabla \cdot (-k_c \nabla c_i) + \boldsymbol{u} \cdot \nabla c_i = R_i \quad (4)$$

Eq. 4 is the transport equation for diluted species including Fick's law for the diffusion of an element $\left(\nabla \cdot (-k_c \nabla c_i)\right)$ with the addition of an advective term $(\boldsymbol{u} \cdot \nabla c_i)$ to account for motions within the fluids. c_i is the concentration of element *i* in the phase of interest, k_c the diffusion coefficient and R_i the reaction rate for element i.

In our case, there are no external sources of elements (N_i=0, Fig. 2).

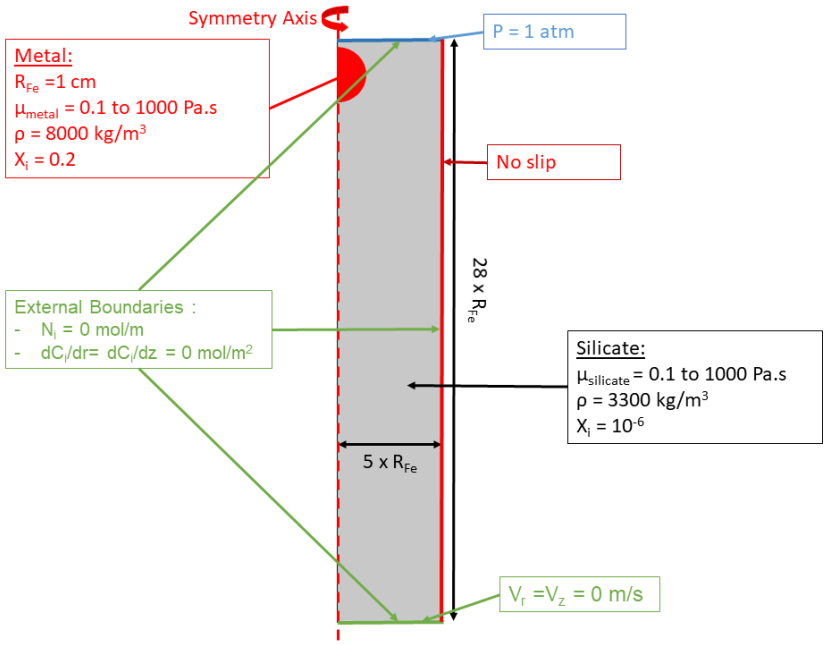

Figure 2: Schematic representation of the initial conditions and geometry of our models. The characteristics of the metal and silicate phases are listed respectively in red and black. The boundary conditions are detailed in blue (top), solid red line (side), green (bottom and global conditions). The red arrow illustrates the symmetry axis (red dotted line) used to define the 3D output.

We assumed the diffusion coefficient (k_c) to be the same for both phases, and independent of the partition coefficient (D_i). Therefore we defined two functions to describe the behavior of element *i* in each phase. One function (X_i^{sil}) describes the behavior of element *i* in the silicate, and therefore tends toward 0 when $\Phi = 1$, the other (X_i^{met}) described the behavior of element *i* in the metal and tends toward 0 when $\Phi = 0$. The combination of the two functions give us the global concentration of element *i* in our computational domain. The link between the two functions, the partitioning coefficient and the phase field is made by defining a reaction at the interface between the metal and silicate (i.e. when $\Phi = 0.5$): R_i is the reaction rate necessary to reach the chemical equilibrium defined by the metal-silicate partition coefficient of element i (D_i). D_i is the Nernst partition coefficient given by $D_i = \frac{X_i^{met}}{X_i^{sil}}$, where X_i^{met} is the mass fraction of element i in the metallic phase, and X_i^{sil} the mass fraction of the same element in the silicate phase at equilibrium. R_i is given by Eq. 5:

$$\frac{dc_i}{dt} = R_i \qquad (5)$$

Where c_i is the concentration in either silicate or metal in mol.m^{-3}, obtained from the density of the phase where the element is ρ^{phase} (for either a metal or silicate phase), the molar mass of the element (M_i) and the mass fraction of the element i in the phase considered is represented by $c_i = X_i^{phase} \rho^{phase} / M_i$. R_i is automatically calculated in a

263 stationary state from the initial conditions and a given partition coefficient so as to reach
264 equilibrium using COMSOL's in-built solver before the simulation. The reaction rate is
265 high enough to maintain the equilibrium between two calculation steps: the typical time
266 for equilibration is 10^{-5} s, which is less than the time step solved by solver**.** R_i is negative
267 when removing siderophile elements from the metallic phase, and positive when creating
268 the same element in the silicate phase. The reaction function is only defined for the
269 metal/silicate boundary, given by the condition $\Phi = 0.5$. The higher the value of $D_i^{met/sil}$,
270 the closer the conditions are to equilibrium, and the lower the reaction rate (R_i) will be.
271 For the domain where $\Phi = 0$ or 1, the equilibrium is set to 0, and therefore the reaction
272 rate is 0. For a given time step, the in-built COMSOL Multiphysics 5.0 solver calculate
273 the Navier-Stokes equations (Eqs. 1 and 2) using finite element method, yielding the
274 velocity field. Then the level-set equation is computed at the same time the advection-
275 diffusion (Eq. 4) equation is solved by finite-element methods on the entire computational
276 domain, with the reaction R_i only defined where $\Phi = 0.5$. The results of the calculation
277 are then used as starting condition for the next time step.
278

279 **2.3.** *Geometry, mesh and initial conditions*

280 First, we defined a geometry for the simulation, using one of the defined boundaries
281 for the eulerian solver available with COMSOL Multiphysics 5.0 software geometries.
282 The best choice for our type of simulation would have been be a 3-D model with a falling

sphere inside it, so as to compare our simulation to analog simulations (Deguen et al., 2011, 2014; Wacheul et al., 2014). Since this type of simulation is very costly in terms of computational time, especially for fluid flow simulations, we used a 2D-axisymetric geometry, which solves the equation on a 2D surface, and uses the symmetry conditions to give a 3D output. This is a good compromise between a 2D and 3D simulation when the diapir is not fragmented. Our simulations focused on a weakly deformable falling sphere (i.e. no break up) with a radius of 1 cm in a cylinder whose diameter was set during the calibration of the simulation.

The geometry and boundary conditions used in this study are presented in Fig. 2. In this geometry, a rotational symmetry axis is defined. For the fluid flow, the boundaries of our calculation domain are characterized as follows:

- on the top boundary, the condition is given by P= 1 atm,
- on the bottom boundary, the condition is set to be a null velocity field
- on the side boundary, the condition is a no slip condition
- on all the boundary there is a no flow condition for the level set equation.

The conditions for chemical diffusion is a constant budget in chemical elements throughout the numerical simulation, i.e. no elemental flux ($N_i = 0$), inward or outward, is allowed on all the external boundaries.

For our calculation domain we used a fixed mesh of triangles, with three main parameters: h_{max}, h_{min} and a curving parameter. The h_{max} parameter gives the maximum size of the triangle side, h_{min} gives the minimum size and the curving parameter gives the arc interception for curving triangles at spherical boundaries. The parameter controlling the accuracy and the computation time for the calculation is h_{max}. The best value for this parameter was determined in the resolution study, see Section 2.4.

The initial conditions are described in Fig. 2. The viscosities were varied for each simulation, but the geometry of the set-up, the initial concentrations, the densities and the droplet radius were kept constant. To avoid numerical instabilities inherent in $X_{sil}^0 = 0$ %wt , the initial concentration was set to $X_{sil}^0 = 10^{-4}$ %wt for the silicate with a density $\rho_{sil} = 3300$ kg.m^{-3}; and $X_{met}^0 = 20$ % wt for the metal with a density $\rho_{met} = 8000$ kg.m^{-3}. The radius of the droplet was $R_{Fe} = 1$cm, falling in a cylinder with a 5 cm radius and a 28 cm height, with the center of the droplet placed initially at 26 cm height.

2.4. Tests of the COMSOL simulation

To correctly set up the computational domain in terms of size and mesh, two effects need to be accounted for:

(1) Grid resolution, which has to be sufficient to capture the physics of small droplet deformation.

(2) Boundary effects, to avoid a major influence of the outer border of the domain on the flow and the generation of artifacts in the velocity field.

To minimize the numerical diffusion of iron during the diapir's descent, we tested several maximum sizes for the mesh grid component $h_{max.}$ Fig. 3 illustrates the time evolution of the ratio between the calculated volume over the theoretical volume of one droplet (given by $V_{theoretical} = \frac{4}{3}\pi R_{Fe}^3$ with R_{Fe}=1cm) for h_{max} values ranging between 0.06 and 0.2 cm. The simulations were performed using the same initial geometry as in Fig. 2, with a silicate and a metal viscosity of 100 Pa.s (corresponding to a Reynolds number of ~2. 10^{-3}, see Eq. 6) and no chemical component to solve. The precision of the calculation increased as the mesh size decreased, especially when there was deformation. On the other hand, the smaller the mesh grid components were, the longer it took to complete the calculation. As can be seen in Fig. 3, the precision is better for a mesh component size of 0.1 cm than for smaller (0.06 and 0.08 cm) or larger (0.2 cm) mesh component sizes. In addition, a maximum component size allowed a calculation time of a few hours (~ 6 hours), whereas a mesh grid size of 0.06 cm yielded calculation times from a dozen hours to 2 days for the less viscous flows. Therefore, for the rest of the study, we used a maximum size of 0.1 cm for the mesh grid (i.e. $R_{Fe}/10$). The mesh size could be adapted to the type of flow for each simulation: for example, for a higher degree of diapir deformation during the simulation

339 (typically for less viscous flows), the mesh size had to be decreased to avoid numerical
340 artifacts. To increase the precision, COMSOL also made it possible to set a minimum size
341 for the mesh grid component so as to get an adapted mesh, with smaller elements at the
342 interfaces between the two phases, and larger elements as the distance from the interface
343 increases. Varying the parameter h_{min} did not affect the simulation for a given value of
344 h_{max}, so it was kept at a constant value of $h_{min} = h_{max}/40$.

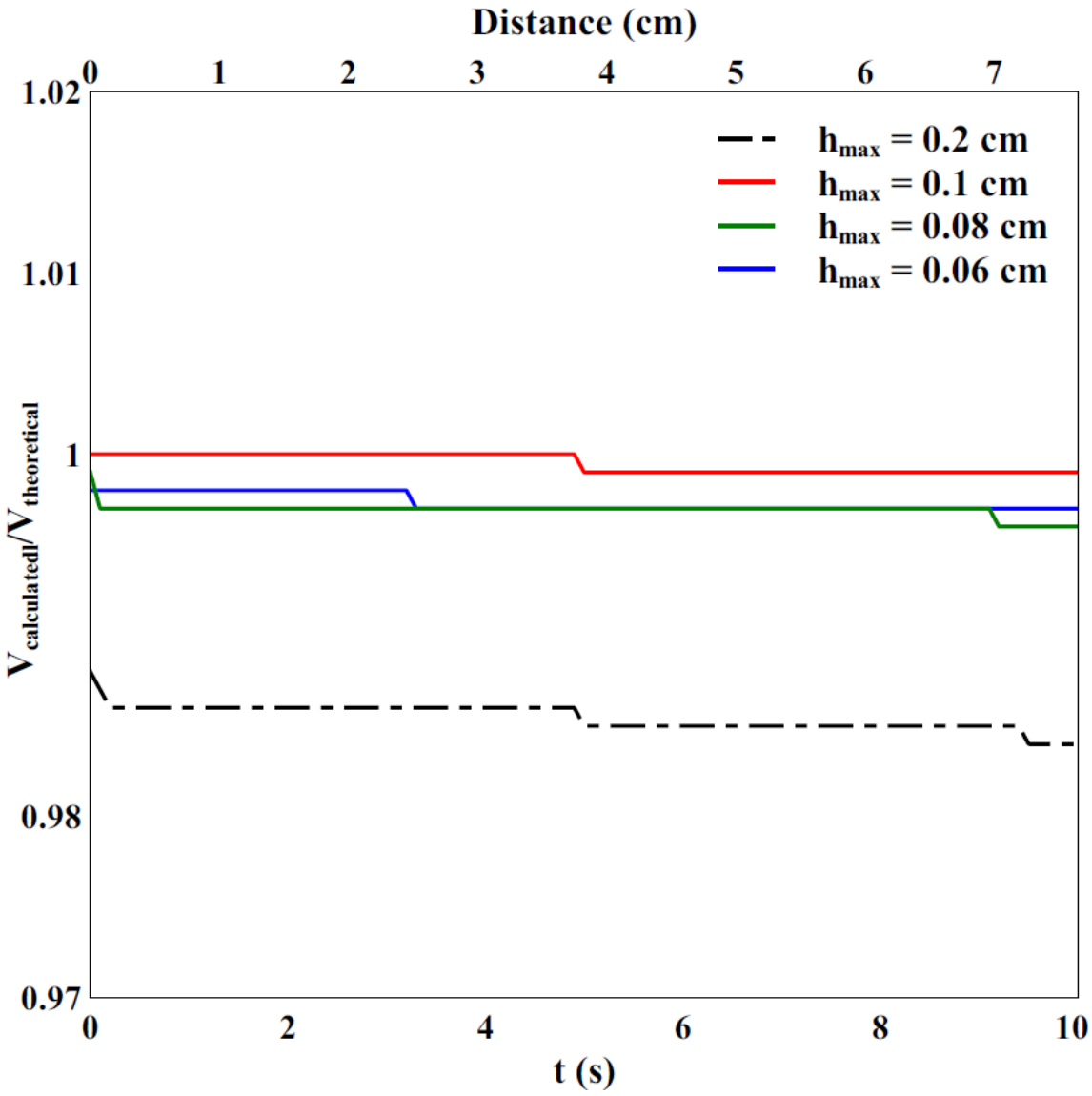

345

346 **Figure 3:** Evolution of the metallic volume ratio ($V_{calculated}/V_{theoretical}$) during a simulation
347 for different h_{max} values, for a silicate viscosity of 100 Pa.s. The colored and dashed line
348 represent the evolution of $V_{calculated}/V_{theoretical}$ for different mesh sizes with time. The scale
349 at the top shows the distance traveled by the diapir over a given time.

350 The second point was to avoid boundary effects on the fluid flow during the simulation.
351 We tested several domain sizes and checked the different velocity field components (r-
352 and z- components). We chose a height equal to $28xR_{Fe}$ and a width equal to $5xR_{Fe}$ which
353 was sufficient to avoid the recirculating flow associated to the descending diapir having a
354 large effect on the velocity field (Fig. 4), while keeping computational time within
355 reasonable bounds. This size of domain still affected the velocity of the diapir (Chang,
356 1961 and Fig. 4). Fig. 4 shows that increasing the width to $6x\ R_{Fe}$ changed the velocity
357 field, albeit very slightly, which indicates a diminution of the wall effect: the mean
358 velocity of the diapir increased by 8 % compared to the mean velocity for a width of $5xR_{Fe}$.
359 However, increasing the width of the domain from $5xR_{Fe}$ to $6xR_{Fe}$ led to a significant
360 increase in computational time (by at least 46 %). Given the limited effect of increasing
361 the domain width and the significant effects on the computational time, we considered this
362 smaller width to be suitable for the study. We applied the same reasoning to choose the
363 height of our domain. To test the resolution of the diffusion in Eq. 4, we benchmarked the
364 validity of the COMSOL solver against steady and unsteady analytical solutions for
365 diffusion problems (Crank, 1975). To test the advective part, we compared the flow
366 velocities from our models with those velocities obtained by Samuel (2012) (see section
367 3.2). Our results showed an acceptable agreement, despite a large discrepancy between
368 theoretical results and observed velocities (45% for the largest one) for flows with the
369 largest velocities, i.e. in the intermediate regime. To explain the observed differences, we

calculated the mesh Peclet number Pe_{mesh} after each simulation with $Pe_{mesh} = \frac{vh_{max}}{k_c}$, where v is the velocity of the diapir, h_{max} is the mesh size and k_c is the diffusion coefficient (10^{-6} $m^2.s^{-1}$, which is higher than a typical chemical diffusion, but high enough to limit numerical diffusion (see Qaddah et al., accepted manuscript). In the reference case and for the other cases within the Stokes regime, the value of Pe_{mesh} was sufficiently low (Pe_{mesh} < 10) meaning that numerical diffusion was negligible (see Mittal & Jain, 2012). For the cases within the intermediate regime, Pe_{mesh} was higher (Pe_{mesh} > 50), which indicates possible numerical diffusion that likely affected our results. To correct this effect a much smaller mesh size would have been necessary. However, the mesh size necessary to prevent numerical diffusion in our models would have led to unreasonable computational times. Therefore, for the lowest viscosity used in our models some error calculations might have occurred in our results, but are negligible in the final model (see Section 5 and 6).

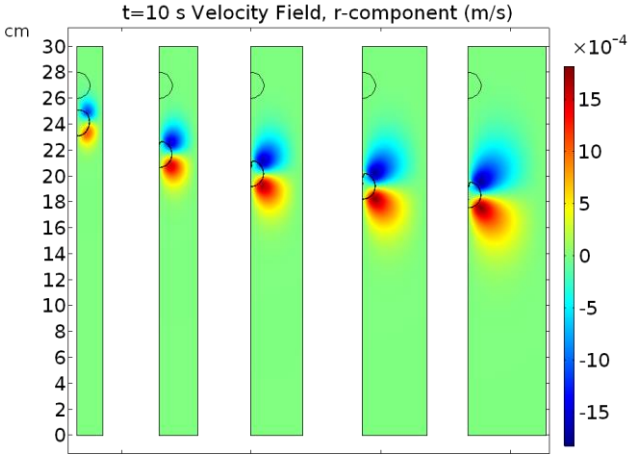

383

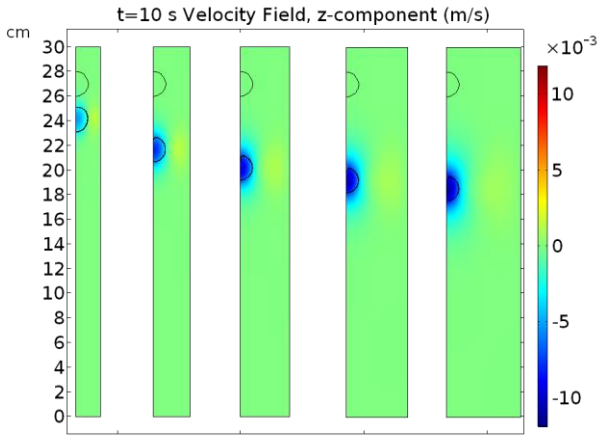

384

385 **Figure 4**: Evolution of the velocity field, r-component (on the left) and z-component (on
386 the right), for different widths of computational domain. Widths vary from 2x R_{Fe} to 6x
387 R_{Fe}. The chosen width for the simulations is 5xR_{Fe}. Note that the results presented here
388 are calibration runs, with a height of 30x$R_{Fe.}$ The same simulations have been performed
389 at varying heights, leading to a final height of 28x R_{Fe} (see Figure 2 for the calibrated
390 geometry).

3. Results

In this section we present the results of our simulations as well as a definition of the non-dimensional numbers and parameters used to interpret the results of the simulation in terms of degree of equilibrium. A reference run was arbitrarily defined to set a reference time evolution for the non-dimensional parameters. Then we varied the viscosity of the silicate and metallic phase for a given partition coefficient value, and finally we varied the value of the partition coefficient for a given viscosity.

3.1. Reference case and characteristic non-dimensional numbers

In this section we present the results for a reference case, where $\mu_{sil} = \mu_{met} = 100$ Pa.s. The temporal evolution of the reference case flow is presented in Fig. 5. This figure shows that for this case both the diapir deformation and the numerical diffusion are weak. The metallic droplet moves a distance of $10 \times R_{Fe}$ (10 cm) in 12.1 seconds.

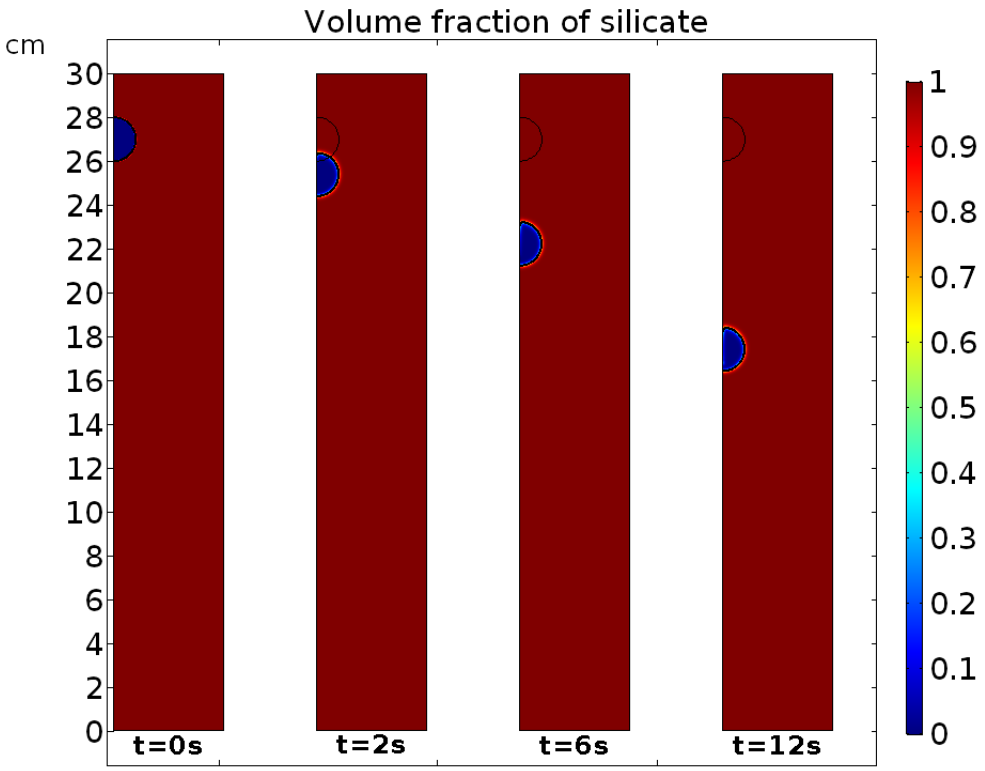

406

407 **Figure 5:** Evolution of the volume fraction of the silicate during the simulation. When
408 equal to 1 (red), the fluid is a silicate, when equal to 0 (blue) the fluid is a metal. The limit
409 between metal and silicate is the black line between the red and blue parts ($\Phi_{ls} = 0.5$). The
410 time necessary for the diapir to reach the distance of $10R_{Fe}$ is 12.1 s.

411

To compare this flow to other flows with different viscosities, we need to use non-dimensional numbers. Since this study focuses on the viscosity variations and the characteristics of the flow, the Reynolds number (*Re*) is the more adequate non-dimensional number, which is given by Eq. 6:

$$Re = \frac{\rho_{sil} R_{Fe} v_{diapir}}{\mu_{sil}} \quad (6)$$

where ρ_{sil} is the density of the surrounding silicate, R_{Fe} is the initial radius of the diapir, v_{diapir} is the velocity of the diapir and μ_{sil} is the silicate viscosity (see Table 1). This number expresses the ratio of inertial forces to viscous forces. When $Re < 1$, the flow is considered to be a Stokes flow, which means that diapir deformation is limited during the descent. When $1<Re<500$, the flow is an intermediate flow between Newtonian and Stokes flow (Samuel, 2012). In our study, we did not investigate the case of $Re > 500$, which is a highly turbulent Newtonian flow.

The velocity of the diapir is strongly governed by the viscosity of the surrounding silicate, which affects the value of *Re* (*e.g.* Samuel, 2012, and references therein). In order to compare different values of the viscosity ratio $R_\mu = \mu_{met} / \mu_{sil}$, we defined the reference

time for each **calculation** as the time necessary for a metallic droplet with radius R_{Fe} to move through a distance $d=10\times R_{Fe}$.

The other non-dimensional number which controls the flow is the Weber number (*We*), which is the ratio of the inertial forces on the surface tension:

$$We = \frac{\rho_{sil} v_{diapir}^2 R_{Fe}}{\sigma} \quad (7)$$

with σ the surface tension (see Tab. 1 for value). The break-up of the diapir is controlled by the Weber number (Wacheul et al., 2014). When $We < 6$ the diapir is stable in Stokes and intermediate flows, and when $We > 6$ the surface tension is no longer high enough to prevent the diapir breaking up (Wacheul and Le Bars, 2017). In this case and in the rest of the present study, the diapirs are always stable with $We < 6$. For the reference case, the diapir velocity is about $v_{diapir} \approx 8\times10^{-3}$ m.s^{-1}. This velocity yields low values of *Re* and *We* (2.2×10^{-3} and 1.2×10^{-3}, respectively), which explains the diapir's stability during its descent (see Fig. 5).

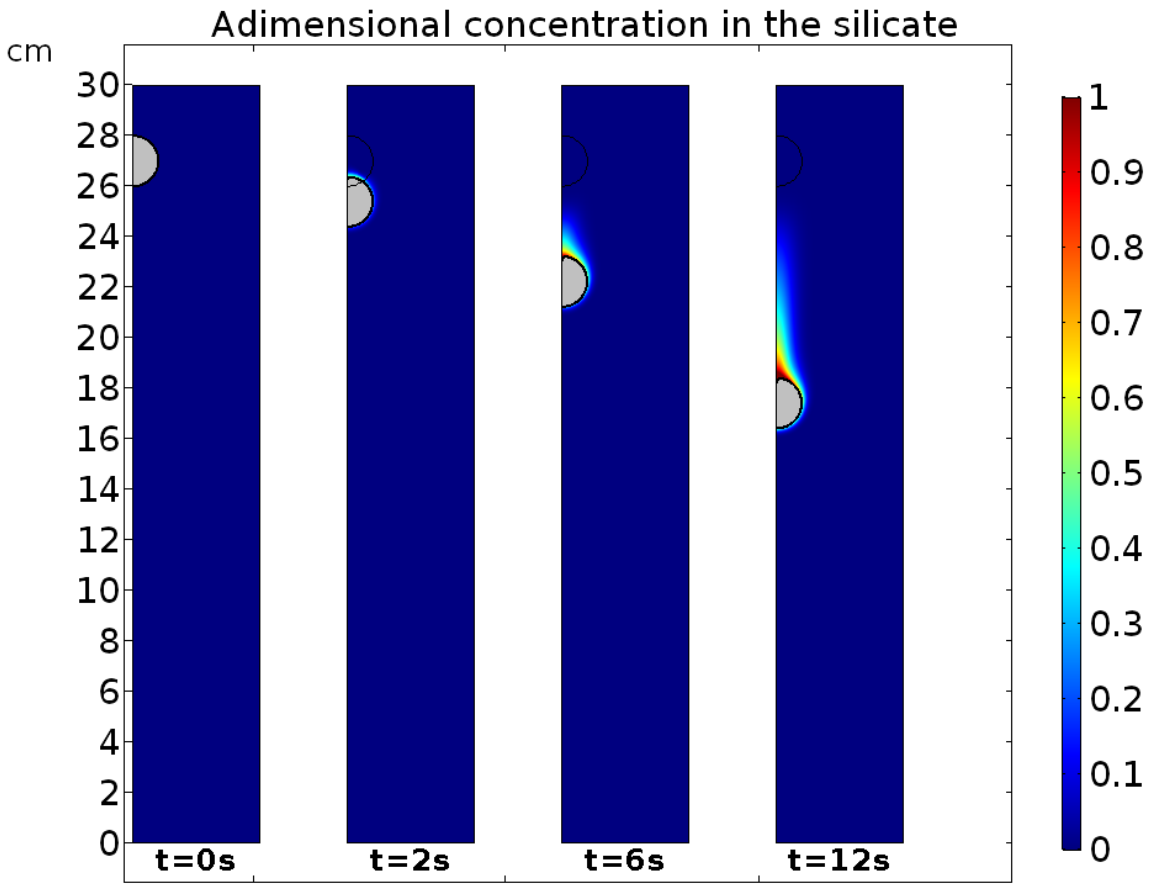

Figure 6: Evolution of adimensional concentration of the siderophile element in the silicate, for a partition coefficient $D^{met/sil} = 1$. For clarity purposes the metal is shown by the grey area surrounded by a black line. The black line is the boundary between metal and silicate and defines the surface where the exchange reaction happens. The adimensional concentration is given by the following formula given in Eq. (9). In this case $X^0_{sil} = 10^{-5}$, $X^0_{met} = 0.2$ and $D^{met/sil} = 1$, and the chemical Peclet number is Pe~800**.**

To study the chemical equilibrium between metal and silicate, we calculated a non-dimensional concentration, or more precisely a non-dimensional mass fraction termed *X'*. This non dimensional mass fraction was calculated so as to satisfy three conditions:

(i) If there is no change in the initial concentration in the silicate, *X*' is equal to 0 (no equilibrium at all)

(ii) If equilibrium is reached, *X*' is equal to 1.

(iii) *X'* is proportional to the concentration in the silicate ($X' \propto X$)

The first condition is reached if $X = X_{sil}^0$. Therefore *X*' = 0 implies a null numerator for *X'*, i.e. $X' \propto X - X_{sil}^0$. For the second condition, it is reached if $X = {X_{met}^{eq}}/{D^{met/sil}}$, by definition of the partition coefficient, where X_{met}^{eq} is the concentration of the element in the metallic phase at equilibrium. In our case, the element is a siderophile ($D^{met/sil} \geq 1$) and the initial concentration is high ($X_{met}^0 = 0.2$). Therefore, at the end of the simulation we could approximate the equilibrium concentration by $X_{met}^{eq} \sim X_{met}^0$. Satisfying the condition *X*' = 1, with $X' \propto X - X_{sil}^0$ and the non-dimensionality of *X*' yield to the following formula given in Eq. 8:

$$X' = \frac{X - X_{sil}^0}{X_{met}^0 / D^{met/sil} - X_{sil}^0} \quad (8)$$

X' is a useful parameter for tracking the evolution of concentration in a particular case, but it is not enough to quantify how much of the silicate is affected by a change in concentration. Moreover, this parameter is not suitable for comparing different studies,

because it is strongly affected by the duration of the sinking. The evolution of the non-dimensional concentration, X', in the reference case is shown in Fig. 6. Equilibrium in the silicate is reached when $X' = 1$ (area in red). This area forms a very narrow zone around the diapir, and most of the silicate is not chemically equilibrated with the metal, because the simulation run time is not long enough.

The parameter R_C is the ratio of the silicate volume that has reacted with the metal to the total volume of silicate. The definition is $R_c = V_{reacted}^{sil}/V_{total}^{sil}$, where $V_{reacted}^{sil}$ is the volume of silicate where $X > X_{sil}^{0}$; meaning R_C is the volume fraction of silicate that has reacted with the metal. To visualize how the ratio is calculated, a representation of the integrated volume is shown in Fig. 7. In this figure, the areas colored in red represent the volume of silicate that has evolved in terms of chemical composition, while the areas in blue represent that which has not been contaminated by the diapir's descent

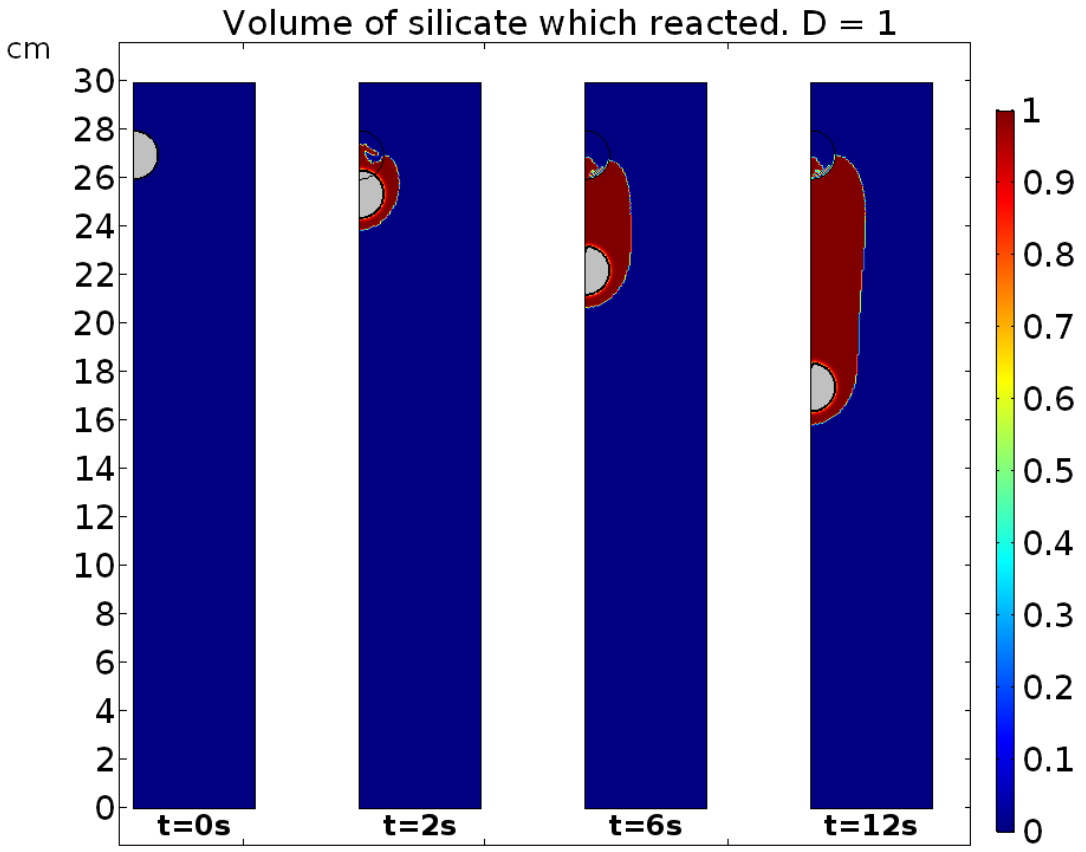

485 .

486 **Figure 7:** Evolution of the volume of silicate undergoing reaction during the simulation.
487 In red, the volume of silicate affected chemically. In blue, the volume of silicate unaffected
488 by the passage of the diapir. The metal is colored in grey. The ratio R_C defined in the study
489 corresponds to the volume of the red areas divided by the total volume of silicate (red +
490 blue areas).

491

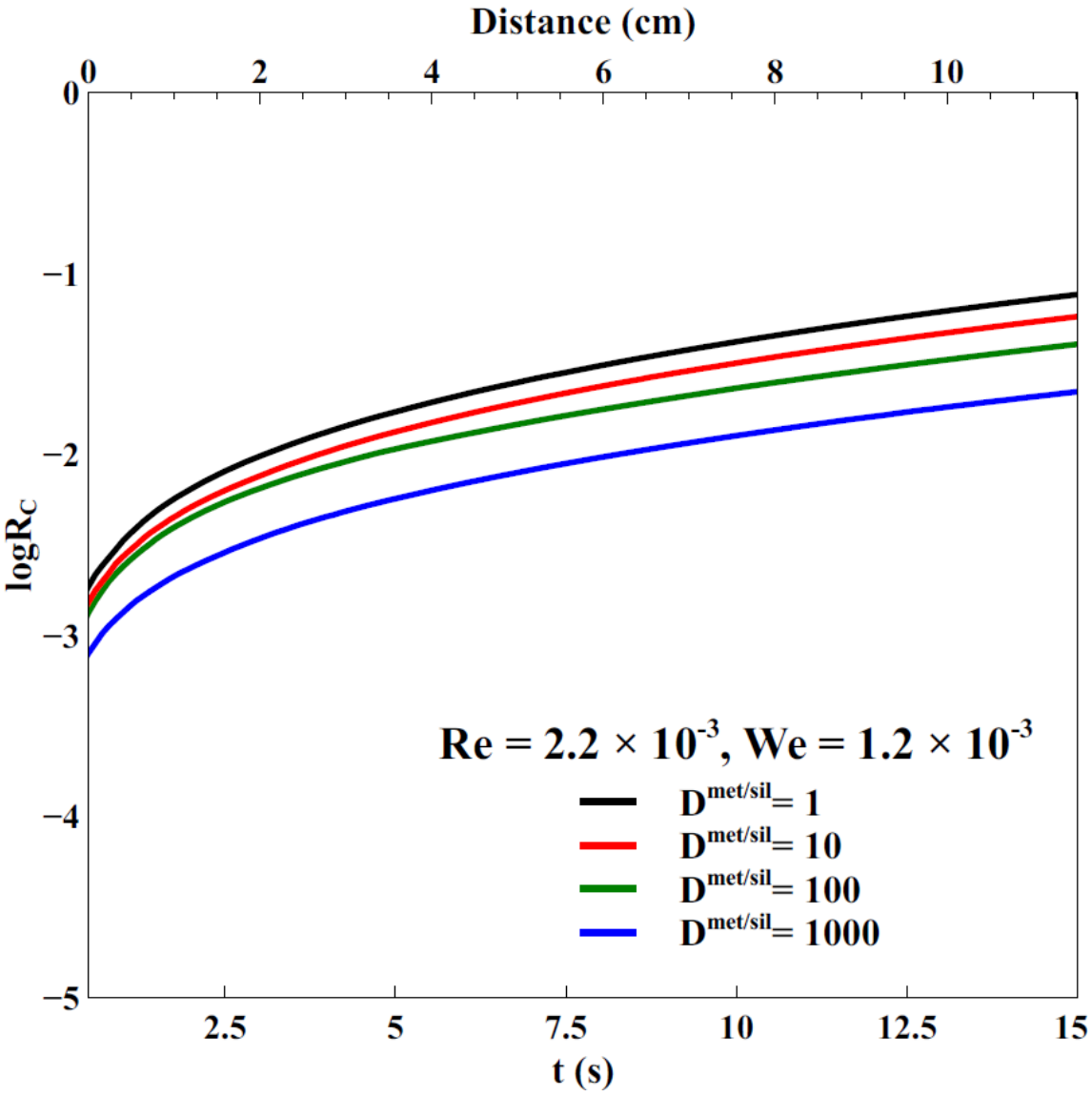

492

493 **Figure 8:** Evolution of R_C as a function of time in the reference case defined in the text

494 ($\mu_{sil} = \mu_{met} = 100$ Pa.s). The four lines illustrate four different values of $D^{met/sil}$ ranging from

495 1 (black) to 10^3 (blue).

496

For each simulation, the volume chemically affected by the diapir's descent increases with time. The time evolution of the R_C value for the reference case is shown in Fig. 8. R_C is increasing with time following the same trend in each case. The difference is in the absolute values of $D^{met/sil}$: the more elevated the value is, the closer the initial conditions are to equilibrium conditions, which leads to a lower reaction rate.

3.2. Range of *Re* and *We* values

The aim of our models was to constrain the influence of the viscosity contrast between the silicate and metallic phases. This led to a wide range of *Re* and *We* values in our numerical simulations. The viscosity of the silicates surrounding the metal droplet controls the flow regime and the sinking velocity. The evolution of the time necessary to reach the distance of $10 \times R_{Fe}$, which depends mostly on the silicate viscosity (Samuel, 2012 and references therein), is presented in Fig. 9. The higher the viscosity of the silicate, the longer it takes for the diapir to reach a set distance. The changes in flow regime result in different expressions for the diapir velocity. In our study, the range of *Re* values only allows Stokes regime flows ($Re < 1$) or intermediate regime flows ($1<Re<500$), with two different expressions for the diapir's velocity. In a Stokes flow the velocity is given by:

514 $$v_{Stokes} = \frac{2}{9}\frac{(\rho_{met}-\rho_{sil})gR_{Fe}^2}{\mu_{sil}} \quad (9)$$

515 For intermediate flows, the sinking velocity is given by:

516 $$v_{intermediate} = \sqrt[2]{\frac{(\rho_{met}-\rho_{sil})gR_{Fe}}{\rho_{sil}C_D}} \quad (10)$$

517 with C_D the drag coefficient. In our case, the drag coefficient is approximated by $C_D =$

518 $\frac{12}{Re} + 0.3$, following Samuel (2012). From Eq. 10, we can also calculate the velocity in

519 each drop flow regime: Stokes, intermediate, and Newton (e.g. Qaddah et al., 2019). The

520 theoretical times associated with the velocity are compared to the actual times observed in

521 simulations in Fig. 9. It shows a good agreement between theoretical and observed diapir

522 velocity, despite some scatter. This scatter is consistent with the wall effect of our

523 simulations: the variation in velocity observed in the Stokes flow is of the order of 10 %,

524 which is consistent with the variation expected if the wall effect is negligible (see Section

525 2.4). Comparison with the typical equilibrium time from Wacheul et al. (2014) in Fig. 9

526 shows that, except for the intermediate flows, the fall time chosen in our study is long

527 enough to reach full equilibrium (or more than 90 % of equilibrium in some cases) inside

528 the metal, leaving the silicate as the limiting phase for equilibrium. The dispersion of the

529 obtained reference time (Eqs. 8 and 9) in Fig. 9 for a chosen value of μ_{sil} is considered

530 therefore as a negligible discrepancy in the rest of the study.

531

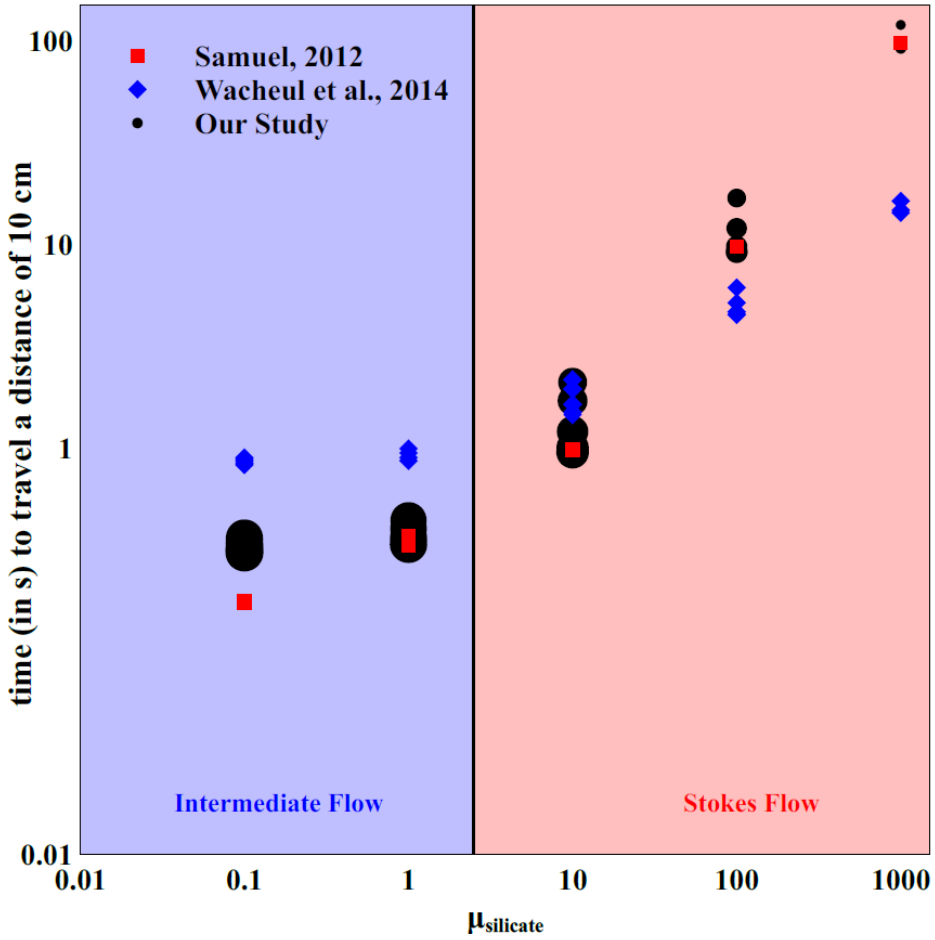

532

533 **Figure 9:** Evolution of the time necessary for the diapir to move through $10R_{Fe}$ as a function
534 of the silicate viscosity. Black points are the values corresponding to each study. The red area
535 corresponds to Stokes flows, and the blue area to intermediate flows. The clusters of black
536 points correspond to the variation in velocity due to the variation in metal viscosity. The
537 theoretical values are plotted in red and derived from equations (9) and (10). Typical times of
538 diapir equilibrium, from Wacheul et al. (2014), are shown in blue. The size of the marker is
539 scaled logarithmically on the chemical Peclet number, ranging from 8 (smallest) to 3000
540 (largest).

In Fig. 10 we plot the *Re* values as a function of the *We* values for each simulation (i.e. for each viscosity contrast used in our calculations). The velocity of the diapir (v_{diapir}) used to calculate *Re* and *We* is determined from our numerical models by the time necessary for the diapir to move through a distance of $10 \times R_{Fe}$. This time is dependent on the viscosity and illustrated in Fig. 9. Fig. 10 (left) shows that in all our numerical simulations, the metallic droplet is stable (i.e. no break up occurs) even though some models are in the Stokes regime and others are in the Intermediate flow regime. In Fig. 10 (right) we compare the range of values with the range of *We* and *Re* values relevant to the geological context of a liquid metallic droplet sinking through a terrestrial magma ocean (Wacheul et al., 2014). As shown in Fig. 10 (right), our range of values is limited compared to possible geophysical values. Larger diapirs leading to high *Re* and *We* values are not considered in our study, which focuses on small droplets in the iron rain scenario.

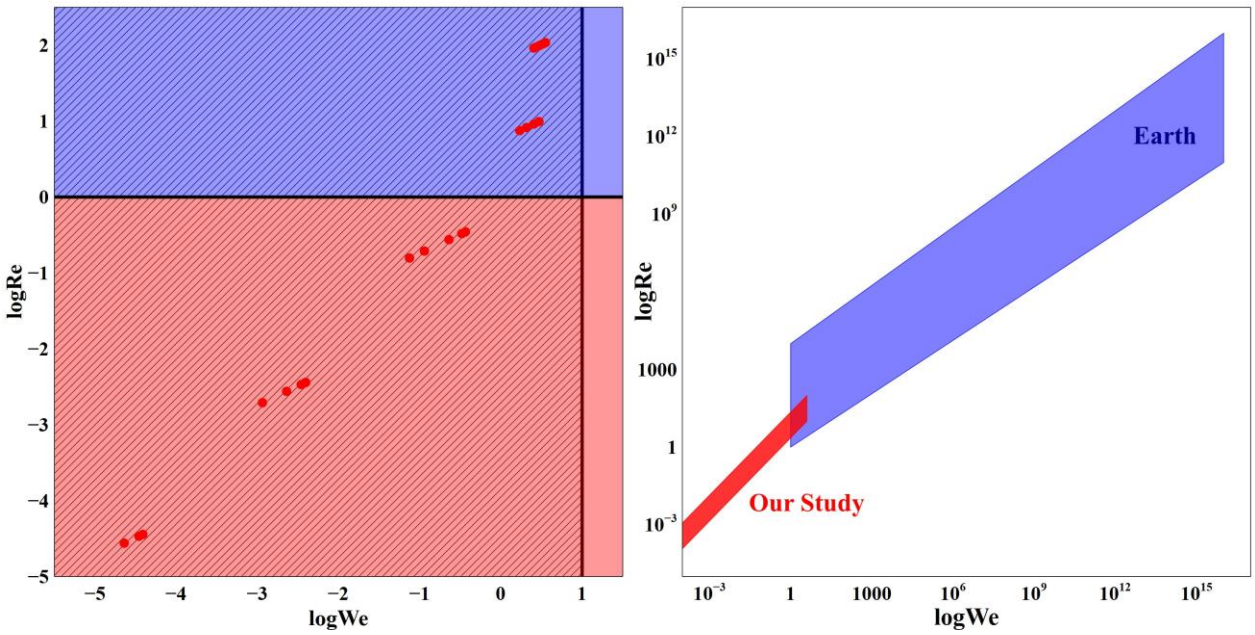

555

556 **Figure 10:** On the left: *Re* as a function of *We* obtained from our numerical simulations
557 (one red circle for each calculation). The blue area shows the Intermediate regime flow,
558 and the red area the Stokes regime flow. The dashed area illustrates the domain where
559 diapirs are stable. On the right: Comparison between the geologically plausible values of
560 *We* and *Re* for the Earth's magma ocean and the values covered by our study.

561

562

563

564 **3.3. Influence of the viscosity ratio**

565 The viscosity ratio is an important parameter controlling the dynamics of diapir
566 descent, both its shape (Qaddah et al., 2019) and stability (Wacheul et al., 2014). In this
567 section, we focus on the influence of the viscosity ratio R_μ $(=\mu_{met}/\mu_{sil})$ by varying the value
568 of the silicate viscosity for a given metal viscosity. Changing the viscosity of metal affects
569 its ability to deform and, hence, its terminal velocity, but this effect is not as strong as the
570 change in velocity implied by a change in ambient viscosity. This behavior is consistent
571 with the equation of diapir velocity in Stokes and intermediate flows (Eqs. (9) and (10)),
572 and is strongly dependent on the silicate viscosity. It is visible in Fig. 9, where a decrease
573 in silicate viscosity from 1000 Pa.s to 10 Pa.s (Stokes flows) leads to an increase in sinking
574 velocity from 10^{-3} m.s^{-1} to 0.1 m.s^{-1} for a metal viscosity of 1 Pa.s. For a constant silicate
575 viscosity of 10 Pa.s, a decrease of the metallic viscosity from 1000 Pa.s to 0.1 Pa.s only
576 increases the velocity from 0.05 to 0.1 m.s^{-1}. The viscosity ratio influences the sinking
577 velocity and, hence, affects the *Re* number and the flow regime, but not as strongly as the
578 silicate viscosity.

579 Fig. 11 illustrates the influence of the *Re* number on the silicate volume chemically
580 contaminated during the sinking of a metallic droplet with R_{Fe}=1cm. For each case, the
581 evolution of R_C is shown as a function of *Re*, and for a distance of 10 cm ($10\times R_{Fe}$). The

582 time corresponding to this distance is shown in Fig. 5 as a function of viscosity. Except
583 for the case with $D^{met/sil} = 10^3$, there is no linear correlation between log(R_C) and log(Re).
584 However, we clearly show a transition between the Stokes regime and the Intermediate
585 regime. In the Stokes regime flow, an increasing Re (i.e. a decreasing value of μ_{sil}) leads
586 to a significant decrease of R_C, while R_C values seem to reach a plateau when the flow
587 reaches the intermediate flow regime. Fig. 11 also shows that the approximation made by
588 Rubie et al. (2003) to achieve an analytical solution for equilibrium is only valid for low
589 Re flows (high silicate viscosity). As the density of the silicate is not significantly altered
590 by the reaction, the parameter R_c (volume ratio of silicate equilibrated) can be compared
591 to their parameter F_s (mass ratio of silicate equilibrated). For the lowest Re value, there is
592 good agreement between our numerical data and the analytical calculation. However,
593 extrapolating the analytical solution to higher Re flows leads to an overestimation of the
594 equilibrated volume.
595

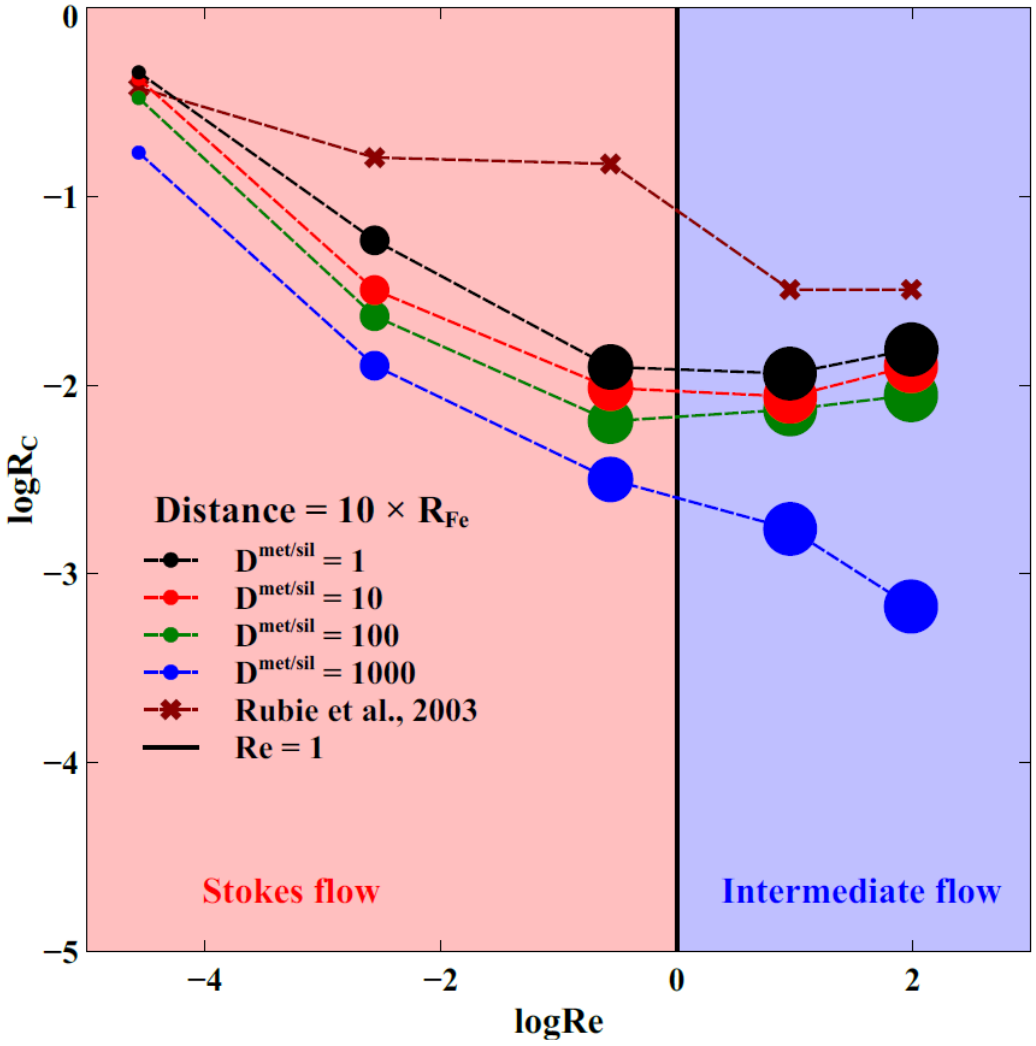

596

597 **Figure 11:** Evolution of R_C as a function of *Re* during the sinking of a 1cm-radius droplet
598 for an adimensional time of 1. The Stokes flow regime (red area) and intermediate flow
599 regime (blue area) are separated by a black vertical line at *Re*=1. The dot color
600 characterizes different values for $D^{met/sil}$ ranging from 1 to 10^3. The size of the marker is
601 scaled logarithmically on the chemical Peclet number, ranging from 8 (smallest) to 3000
602 (largest).

603 The R_C ratio is presented in Fig. 12 as a function of R_μ. A decrease in R_C is observed with
604 an increase in R_μ (i.e. a decrease of μ_{sil}) for a given viscosity of the metallic phase. For the
605 five parts of Fig. 12, which correspond to the five values of μ_{met}, the trend and the
606 magnitude of the values of R_c are quite similar, meaning that the effect of the viscosity
607 ratio is less important than the ambient viscosity, which governs the flow regime. For high
608 values of R_μ, the same plateau phenomenon as seen in Fig. 11 is observed, which
609 corresponds to lower silicate viscosity values (intermediate flow). In the Stokes regime,
610 the sinking velocity scales with μ_{sil}^{-1} (Eq. (9)) while in the intermediate regime, the sinking
611 velocity scales with C_D^{-1}. Given the expression of the drag coefficient (derived from
612 Samuel, 2012; see Section 3.2), and the expression of *Re* (Eq. (6)), the sinking velocity in
613 the intermediate regime scales with $(\rho_{sil}\mu_{sil})^{-0.5}$, as given by Eq. (10). Hence, R_μ has a
614 greater effect on Stokes flows than intermediate flows, because the changes in diapir
615 velocity are more pronounced for Stokes flows, as shown in Fig. 5.
616 Although the evolutions of R_C as a function of R_μ are quite similar in the five panels of
617 Fig. 12, some differences are noticeable. For the lowest values of μ_{met}, the R_C ratio
618 increases at high R_μ values while for high values of μ_{met}, the R_C ratio is nearly constant or
619 decreases with high R_μ (except for $D^{met/sil}$ =1000). This could be explained by the fact that
620 a higher viscosity ratio tends to stabilize the diapir and slow down its descent (Wacheul
621 et al., 2014). In a Stokes regime, it leads to an increase in the time necessary to reach the
622 same distance, in other words a longer reaction time; but in intermediate regimes this time

623 does not change significantly, while the diapir is less deformed, leading to a smaller
624 surface of exchange between metal and silicate. We illustrate this point in Fig. 13, for a
625 silicate viscosity of 0.1 Pa.s: the normalized surface of the diapir varies from 1 to 2.3 with
626 decreasing values of R_μ, which means that low R_μ for high *Re* (~100) values lead to an
627 increase of exchange surface by 130% relatively to the initial diapir surface. The same
628 effect is observed for μ_{sil} =1 Pa.s (*Re*~10), to a lesser degree: for low metallic viscosity
629 (R_μ = 0.1) the diapir surface increases by 20%. This leads to an increase in R_c value for all
630 partition coefficients except for $D^{met/sil}$ = 1000, for which an increase in diapir surface has
631 a negligible effect, the deformation occurring over a short timescale at a low reaction rate.
632 This effect is weak in our study compared to the effect of *Re* and $D^{met/sil}$ (see Section 3.4),
633 because the *We* range of our study does not allow major diapir deformation. For the
634 deformation rate to have a strong impact on chemical equilibrium, the *We* values have to
635 be much higher (We> 10, see Lherm & Deguen, 2018).
636

637

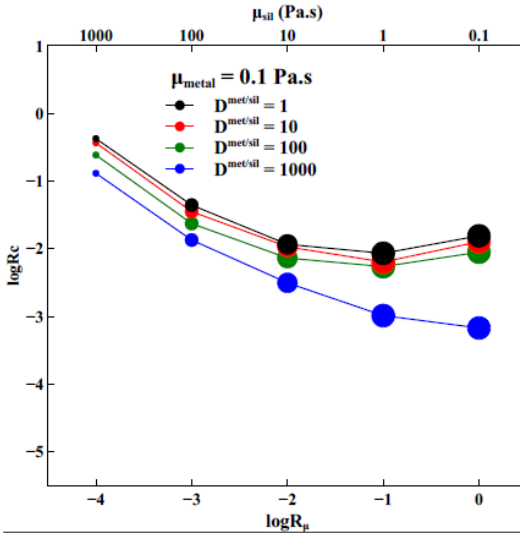
μsil (Pa.s)
1000
100
10
1
0.1
μmetal = 0.1 Pa.s
Dmet/sil = 1
Dmet/sil = 10
Dmet/sil = 100
Dmet/sil = 1000
logRc
logRμ

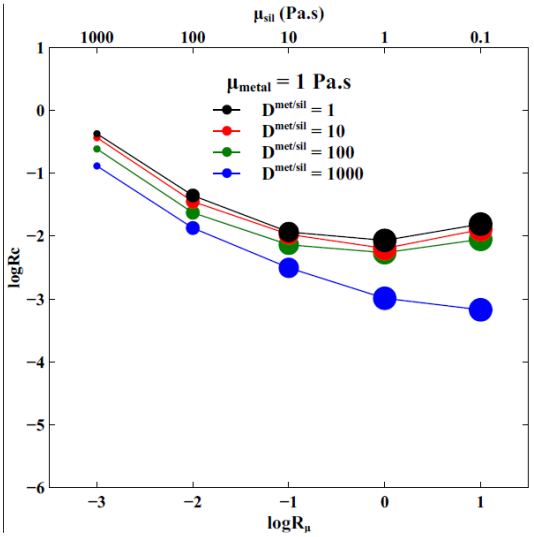
μsil (Pa.s)
1000
100
10
1
0.1
μmetal = 1 Pa.s
Dmet/sil = 1
Dmet/sil = 10
Dmet/sil = 100
Dmet/sil = 1000
logRc
logRμ

638

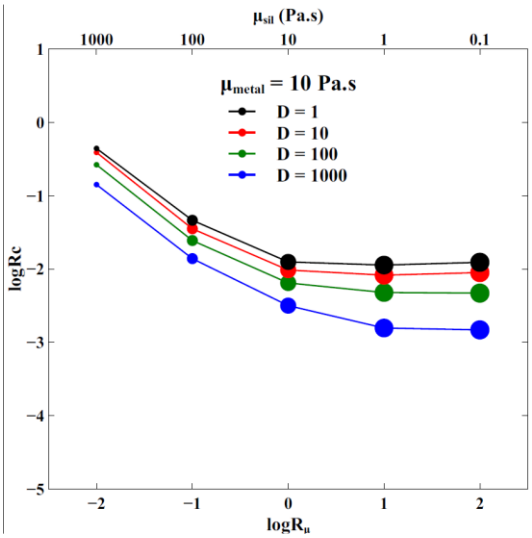
μsil (Pa.s)
1000
100
10
1
0.1
μmetal = 10 Pa.s
D = 1
D = 10
D = 100
D = 1000
logRc
logRμ

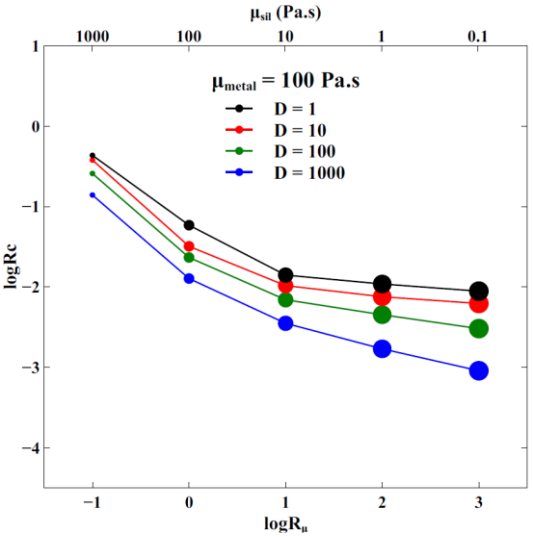
μsil (Pa.s)
1000
100
10
1
0.1
μmetal = 100 Pa.s
D = 1
D = 10
D = 100
D = 1000
logRc
logRμ

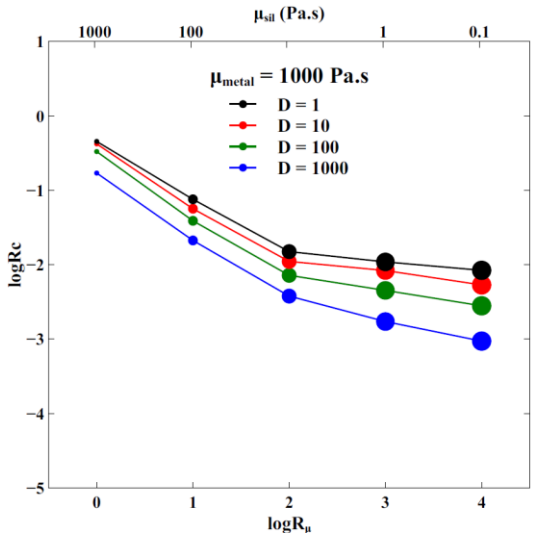

Figure 12: Evolution of R_C as a function of R_μ for 5 different metallic viscosities (shown in the 5 boxes), different values of $D^{met/sil}$ and obtained at a distance of $10R_{Fe}$. From top left to bottom panel the metallic viscosity increases from 0.1 Pa.s to 1000 Pa.s. The silicate viscosities corresponding to R_μ are indicated on the top x-axis. The size of the marker is scaled logarithmically with the chemical Peclet number, ranging from 8 (smallest) to 3000 (largest).

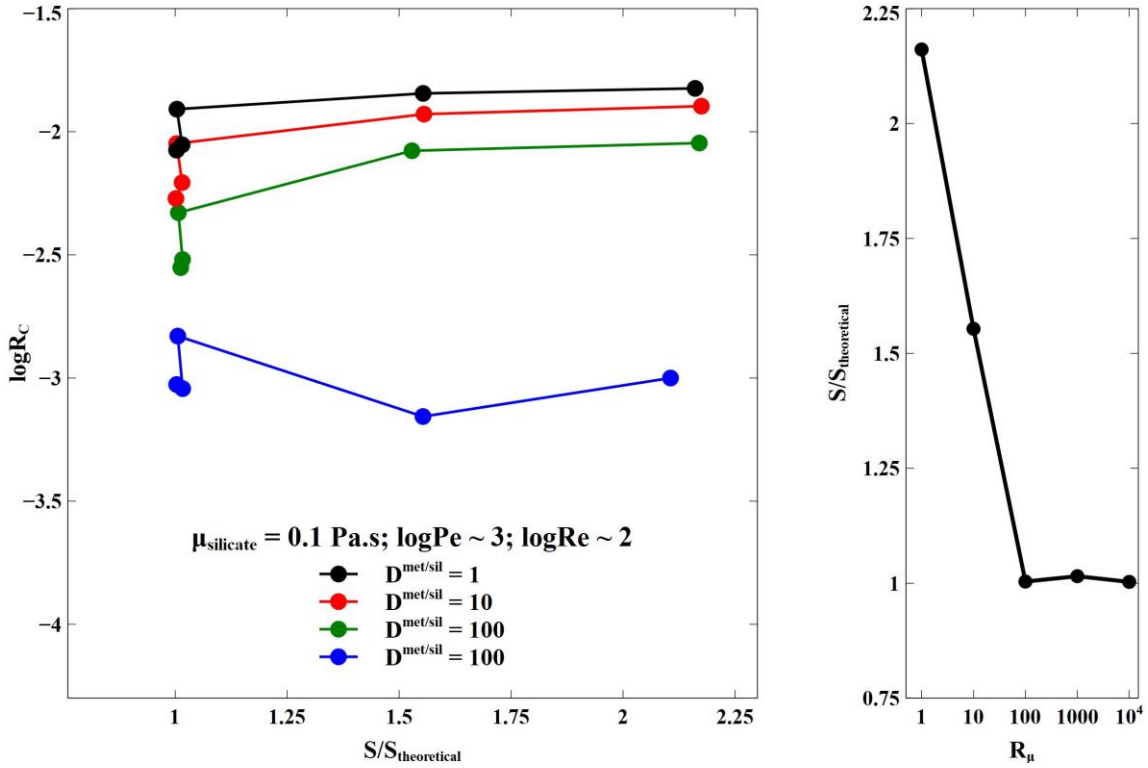

Figure 13: Evolution of log R_C as a function of the normalized surface (left panel) and evolution of the normalized surface as a function of R_μ (right panel) for models with $\mu_{silicate}$ = 0.1 Pa.s for the reference time defined in Fig. 9. The normalized surface of the diapir is the surface of the diapir in the simulation divided by $S_{theoretical} = 4\pi R_{Fe}^2$ (initial surface of the sphere).

3.4. Influence of the partition coefficient

We have shown in Figs. 11 and 12 that chemical equilibration was less efficient when the value of the viscosity ratio between the iron and silicate phases was higher. This conclusion also stands for the whole range of partition coefficients used in our models. As detailed in Section 2.2, the higher the value of $D^{met/sil}$, the closer the conditions are to equilibrium conditions, and the lower the reaction rate (R_i) will be. However, the thermodynamical equilibrium is reached faster, which limits the amount of exchange between the metallic droplet and the surrounding silicate. Therefore, the contaminated volume represented by R_C decreases when $D^{met/sil}$ increases (see Figs. 11 and 12). This effect is relatively small: an increase of 3 orders of magnitude decreases *Rc* by less than one order of magnitude.

3.5. Parameterization of the chemical contamination

As shown in the previous sections, the contamination of silicate by a siderophile element depends on the Reynolds number, viscosity ratio, and the values of metal-silicate partition coefficients. To use our results in an iron rain scenario following an impact during planetary formation, it is necessary to quantify the relative effect of each parameter on

chemical contamination. In section 3.1 and 3.2 we chose a distance of $10\times R_{Fe}$ and the relevant time (Fig. 5) at which R_C is considered to have reached a stationary value. With this assumption the error is limited, since R_C tends to reach a plateau in all our simulations (see Fig. 8). Therefore, we consider the R_C values obtained from our models at a distance of $10\times R_{Fe}$ in our parameterization.

We show in Sections 3.2 and 3.3 that increasing the Reynolds number and viscosity ratio both tend to decrease R_C. In Figs. 11 and 12, $\log(R_c)$ decreases linearly with both $\log(Re)$ and $\log(R_\mu)$ independently of the value of $D^{met/sil}$ with a small error in the prediction ($R^2 > 0.85 - 0.9$). Concerning the effect of partition coefficients, (Section 3.4), all the curves in Figs. 11 and 12 are parallel, showing that there is a linear relationship between $\log(R_c)$ and $\log(D^{met/sil})$. We parameterize the evolution of $\log(R_C)$ as a function of $logRe$, $logR_\mu$ and $logD^{met/sil}$. The method used here is a multi-linear regression fit on all the data retrieved from the simulations:

$$logR_C = a\times logD^{met/sil} + b\times logRe + c\times logR_\mu + d \quad (11)$$

where a, b, c and d are constants fitted to the data by least-square regressions. The values of the parameters are presented in Table 2. As shown in Fig. 14, the parameterization of Eq. (11) shows a relatively good fit to the data retrieved from calculations. This kind of fit is not perfect, and could certainly be improved by including non-linear dependencies. It is also worth noting that this parameterization is valid for a narrow range of Re and We

values, and its precision is lower at high *Re* values (see section 2.4). For instance, different results can be found in turbulent cases (high *Re*, Deguen et al., 2014) and/or with deformed diapirs (high *We*, Lherm & Deguen, 2018). However, this form of equation (Eq. (11)) is practical to use in models of planetary formation with limited error on the value of R_C, therefore we chose this form to simplify the calculations in sections 5 and 6.

Parameters	a (*Dmet/sil*)	b (*Re*)	c (R_μ)	d
Values	-0.235	-0.283	0.011	-1.686
1σ	0.02	0.03	0.001	0.07

Table 2. Values of fitted parameters for Eq. 11 using the least-square methods. The errors associated with the value are given by the 1σ error value. The data used for parameterization are the same as the data presented in sections 3.3 and 3.4. The comparison between calculated values from Eq. 11 and the values obtained after simulation is presented in Fig. 13

This parameterization shows that the main parameters controlling the contamination of a liquid silicate reservoir by a siderophile element during the sinking of a metallic droplet are the Reynolds number and the metal-silicate partition coefficients. The higher the $D^{met/sil}$ is, the less the silicate will be contaminated, which reflects the fact that we consider here a siderophile element. The Reynolds number has the same effect as $D^{met/sil}$: the higher *Re* is, the lower R_C will be. This high absolute value of *b* reflects the

710 importance of the silicate viscosity, which controls the diapir velocity, as well as the type
711 of flow and the deformation of the diapir. The fact that the parameter *b* is negative shows
712 that increasing the value of the Reynolds number will decrease R_C. Indeed, decreasing the
713 viscosity increases the Reynolds number (Eq. 6) as well as the diapir velocity (*e.g.* Samuel,
714 2012; Wacheul et al., 2014, and Fig. 5).
715

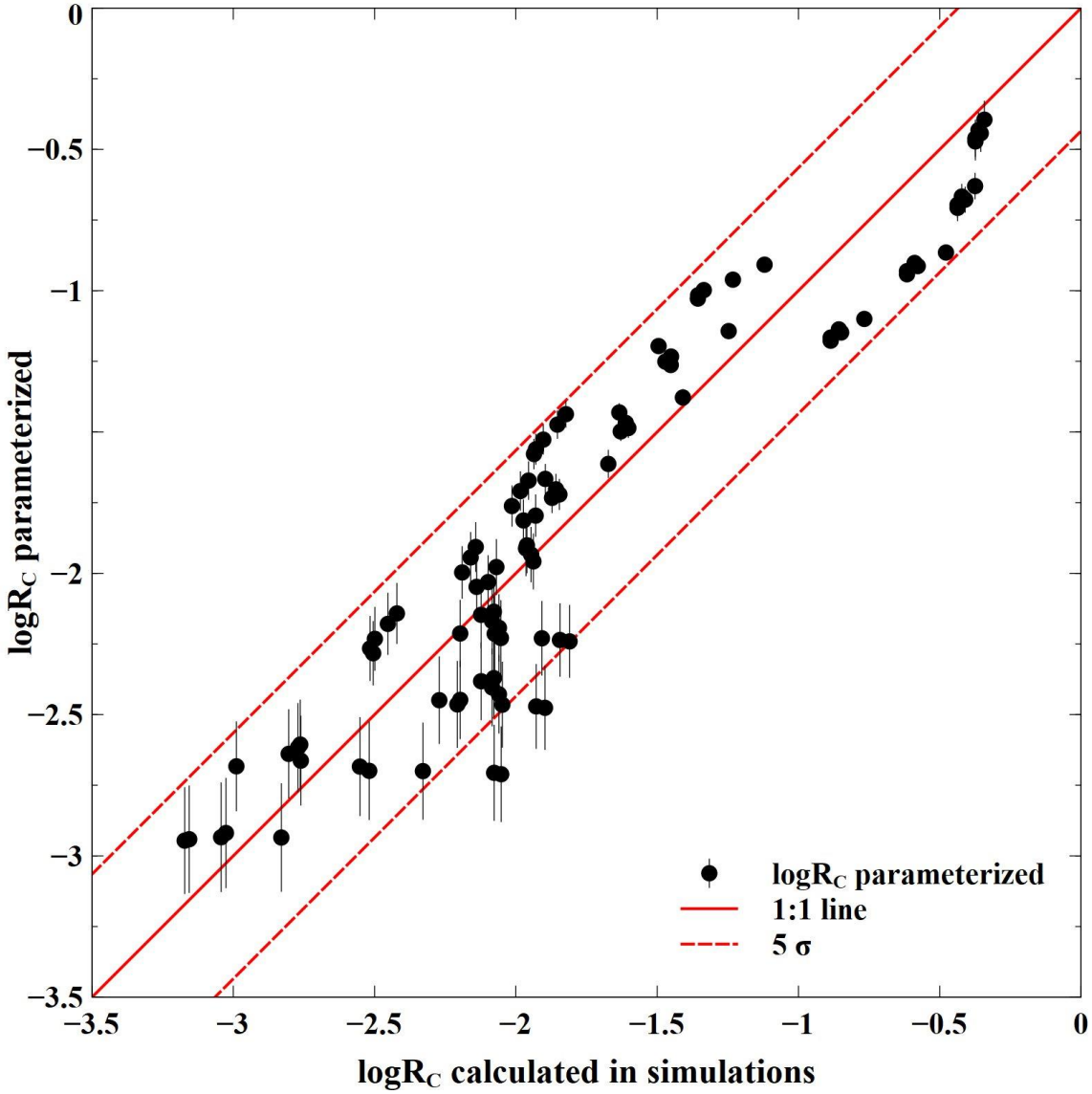

716

717 **Figure 14:** log*Rc* calculated from the parameterization of Eq (11) vs log*Rc* obtained from

718 the simulations. The red line is the 1:1 line (perfect fit), and the dashed lines bound the 5σ

719 confidence interval.

720

4. From a single droplet to the large impact context

In the previous section, we derived a parameterization (Eq. 11) to estimate the volume fraction of a magma ocean contaminated by a unique 1cm-radius metallic droplet. In this section we apply this parameterization to large impacts in the context of late accretion. The parameterization was calculated for a pertinent range of metallic and silicate viscosities. Numerical simulations and laboratory experiments estimated the viscosity of silicate melts at high pressure within the range of 0.01 Pa.s to 1 Pa.s. (Liebske et al., 2005; Karki & Stixrude, 2010; Karki, 2018). This range is stable because the viscosity tends to increase with pressure, but decrease with increasing temperature. As for the viscosity of metallic liquid, few experiments have been made, but the experimental results also show that the range of viscosity for liquid iron alloy is stable, at around 0.01-0.1 Pa.s (Kono et al., 2015). Therefore, the effect of viscosity on the equilibrium rate calculated in our simulation can be extrapolated for a high pressure context in an entirely liquid magma ocean. The higher values (10 -1000 Pa.s) of μ_{sil} tested in our simulation can also be applied at the end of the magma ocean stage when the silicate liquid is starting to crystallize (but before the mushy stage where the flow dynamics is governed by the viscosity of the solid silicate phase).

739 A more limiting factor to the extrapolation of our parameterization to planetary formation
740 is the size of our computational domain. However, it is possible under certain conditions,
741 which are listed below.
742 When a differentiated impactor collides with a growing planet, two fragmentation
743 mechanisms of its metallic core occur. The first fragmentation is induced by the impact
744 itself that stretches and disperses the impactor's core (Kendall and Melosh, 2016). The
745 lunar crater observations showed that the most probable impact angle is $\alpha = 45°$
746 (Shoemaker, 1962). When considering an impactor with a metallic core radius of R_{core}
747 impacting a magma ocean at an angle $\alpha = 45°$, it is possible to apply our parameterization:
748 the dispersion of the impactor's core material becomes the same as our study
749 computational domain. The mantle fraction affected by the impact (i.e. the volume of
750 mantle into which the metallic droplets are initially spread out) can be approximated by
751 the volume of a cylindrical portion with an angle α, a thickness h and a radius L. The
752 volume of mantle affected is then $V_{affected} = \alpha h L^2/2$. For R_{imp}=100 km, R_{core}=50 km,
753 and α=π/4, Kendall & Melosh (2016) give h=200km, L=2000 km: we can then estimate
754 $V_{affected}$ = 3.14 x 10^{17} m^3. After the first fragmentation induced by the impact, a second
755 rapid fragmentation occurs leading to the formation of much smaller droplets of different
756 sizes. Wacheul et al., (2014) showed that metallic diapirs will fragment into droplets with
757 a mean radius of between 4 mm and 20 mm. Assuming an average droplet radius of 1 cm
758 (Rubie et al., 2003) and that all the impactor's core diapir is fragmented into these cm-

radius droplets, an impactor's core with radius R_{core}=50 km will fragment into ≈10^{20} cm-radius droplets. This yields a concentration of 400 droplets/m^3, or 1 droplet per 2.5 liters, which yields a metal/silicate volume ratio of 0.0016 within $V_{affected}$. Currently, no scaling law describes the relation between (L, h, α) and R_{imp} (and as a consequence R_{core}). According to Kendall & Melosh (2016), for R_{core}=50km, L≈40R_{core} and h ≈ 4R_{core} and by making the assumption that these two relations are also valid for different R_{core} values, we can infer that the ratio of the impactor's core volume over the affected volume is constant for any impactor size.

In the numerical models described in the previous sections, we consider a metallic droplet sinking into a large volume of molten silicates to avoid boundary effects. In our study the ratio between the volume of the iron droplet and the volume of the computational domain is 0.0019, which is relatively close to the volume ratio of 0.0016 expected after an impact.

After a large impact, the impactor's core is dispersed within a volume $V_{affected} = \alpha h L^2/2$. Assuming the formation of a cloud of cm-radius droplets with an iron fraction $\chi_{Fe} = 0.0016$ within $V_{affected}$, the volume where chemical exchange between the droplets and the magma ocean will occur is:

$$V_{exch} = R_c V_{affected} \quad (12)$$

Using Eq. (11), Tab. 2 and considering L=40R_{core} and h = 4R_{core} (Kendall and Melosh, 2016), we can calculate the fraction of the volume of the Earth's mantle V_{exch}/V_{mantle} in which chemical exchange is likely to occur. Fig. 15 shows V_{exch}/V_{mantle} as a function of the impactor radius and illustrates the influence of the partition coefficient and the viscosity contrast between the magma ocean and the liquid iron on this ratio.

As the impactor size increases, the mantle volume chemically affected by the impact increases by R_{imp}^3. This relation is constrained by the simple formula we have used to relate $V_{affected}$ to R_{core}. Given the current knowledge of the impact-induced fragmentation mechanisms of an iron core on a planetary scale, this simplification is a first step toward a global understanding of the chemical equilibration occurring after a large impact. Fig. 15 (left) illustrates that an increase in partition coefficient leads to a decrease in the ratio V_{exch}/V_{mantle} in agreement with Eq. (11) and the values from Tab. 2. Fig. 15 (left) shows that for R_{core}=1000 km, increasing the partition coefficient by 2 orders of magnitude decreases the value of the ratio V_{exch}/V_{mantle} by a factor of 3. This effect is significant but less important than the influence of the viscosity ratio. Fig. 15 (right) shows that increasing the magma ocean viscosity relative to a constant liquid iron viscosity of 0.1 Pa.s from 0.1 Pa.s to 100 Pa.s leads to an increase in V_{exch}/V_{mantle} by a factor of more than 5. According to Fig. 15, a very large impact such as that which led to the formation of the

Moon-Earth system, involving a highly viscous magma ocean, would strongly enhance the chemical equilibration between the impactor's core and the Earth's mantle. This result needs to be nuanced, since a large impact is likely to increase temperature and therefore lower the viscosity of the magma ocean.

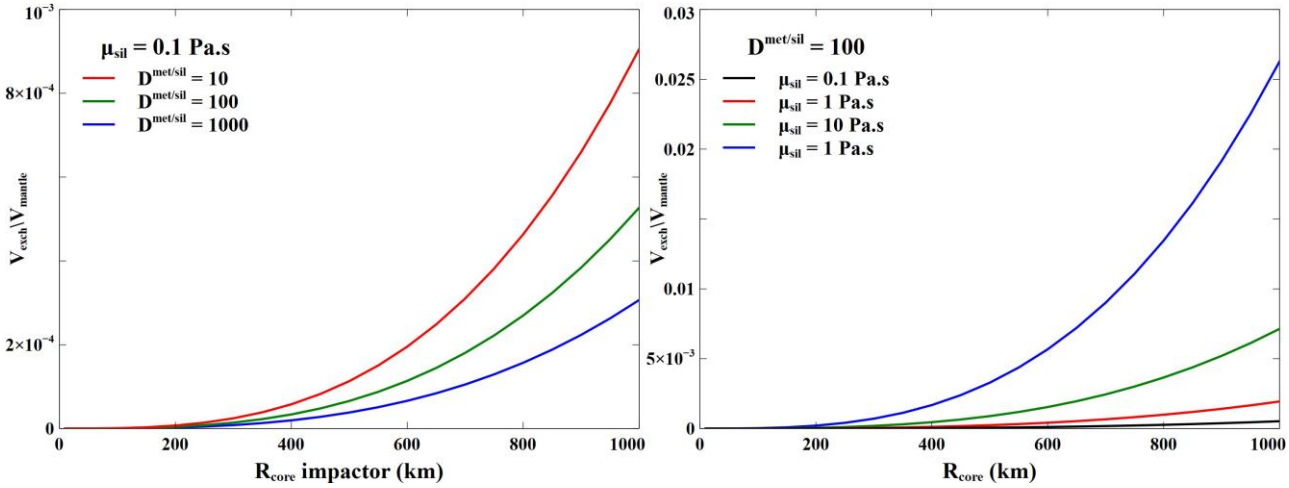

Figure 15: Mantle fraction chemically contaminated by a moderately siderophile element after metallic core fragmentation as a function of the impactor size. In these figures we compute Eqs. 6, 11 and 12 using R_{Fe}=1cm, v_{diapir}=v_{stokes} and μ_{met}=0.1 Pa.s. The left panel shows the influence of the partition coefficient for a fixed viscosity ratio R_{μ}=1. The right panel shows the influence of the viscosity ratio for a fixed partition coefficient $D^{met/sil}$=100.

5. Signature of a large impact on the mantle composition

This section aims at improving previous accretion models (e.g. Fischer et al., 2015, Siebert et al., 2012, Wood et al., 2008) by accounting for a possible chemical disequilibrium at a given depth. Previous models assumed that at a given step in accretion, equilibrium is reached throughout the entire mantle (Wood et al., 2008; Siebert et al., 2012; Boujibar et al., 2014; Clesi et al., 2016). This equilibrium is set by the final pressure on reaching equilibrium, usually at a depth corresponding to 50 % of the core mantle boundary depth (or close to this depth, for instance in Rubie et al., 2015), in order to fit the Ni and Co partitioning behavior (Bouhifd & Jephcoat, 2003;2011; Fischer et al., 2015).

In this section and the following one, the hypothesis is the same as in previous models of accretion, but with the notable exception that not all of the mantle reaches equilibrium. The amount of mantle equilibrated is defined using Eqs. (11) and (12), i.e. our parameterization is applied directly to a classical model of equilibration in a magma ocean, thus adding one step of complexity to previous models.

5.1. Geochemical elements of interest

To estimate the chemical equilibrium between the impactor's core and the impacted mantle, we focus our calculations on the chemical behavior of moderately siderophile elements such as Ni and Co for which $D^{met/sil}$ is strongly dependent on pressure (Bouhifd

& Jephcoat, 2003, 2011; Siebert et al., 2012; Fischer et al., 2015). These two elements are important, since the models of deep magma ocean are designed to explain their relatively high abundances in the BSE (Drake and Righter, 2002). The maximum depth of the magma ocean (around 50% the CMB depth throughout accretion) is derived from the pressure for which the partitioning behavior of Ni and Co yields a 19.05±2 ratio in the BSE (Bouhifd & Jephcoat, 2003, 2011). In the previous sections, we considered a generic, moderately siderophile element with a metal/silicate partition coefficient ranging from 1 to 1000. This range is large enough to extrapolate the trend derived from our simulations to the behavior of Ni and Co at high pressure. For Ni, this partition coefficient ranges between ≈400 for P =1 GPa, and ≈ 20 for 40<P<60 GPa. For Co, the partition coefficient ranges between ≈ 100 for P = 1 GPa and ≈ 20, for 40<P<60 GPa (Bouhifd & Jephcoat, 2011 and references therein). In the models presented below, we assume that the pressure of equilibrium after an impact corresponds to the last stages of equilibrium in a deep magma ocean, at between 50 and 60 GPa (see Appendix B in Clesi et al., 2016 for the corresponding calculations and the full evolution of pressure, temperature and f_{O2} during the accretion) with values of Ni and Co partition coefficients of between 20 and 80 for the corresponding f_{O2}. In the following section, we consider that the iron content of the mantle is close to the BSE content (8% wt) and is not affected by the impact. The f_{O2} is then considered constant relatively to the iron-wüstite buffer and its value is $\log f_{O2} \approx -2$ ΔIW.

In this case, the Ni and Co partition coefficients have converged toward the same value: $D^{met/sil} \approx 20$, which is used in the following calculations.

5.2. Chemical signature of a large impact on the Ni/Co ratio

Here we characterize the effect of a single impactor on the Ni/Co ratio in the mantle. We consider an initially fully accreted Earth. The reference composition of the impacted mantle is set to the BSE composition defined in McDonough and Sun, (1995) (Ni/Co = 19.05, 2000 ppm of Ni and 105 ppm of Co in the mantle). We consider that the silicate fraction of the impactor is lost during impact and that only its metallic core is trapped within the impacted mantle. The impactor has a radius of between 10 km and 1000 km and the same composition as the Earth's core (McDonough, 2003). Given the range of impactor size, the mass accreted is negligible compared to the Earth's mass: with a mean density of 9400 $kg.m^{-3}$, a metallic impactor of 1000 km radius adds a total mass of $\sim 3.10^{22}$ kg, which is 0.5% of the Earth's mass. This choice of size and composition for the impactor allows us to focus on the change in mantle concentration, without changing the final core concentration, especially the light element (Si and S) content, in the core. Furthermore, this impactor composition, and its relatively low mass, would not significantly change the oxygen fugacity and thus does not affect the partitioning behavior of Ni and Co.

This section aims at characterizing the partitioning behavior of Ni and Co as a function of the impactor radius and the viscosity contrast R_μ computing Eqs. (11) and (12). The first term of Eq. (11) illustrates the influence of the partition coefficients for Ni and Co. These partition coefficients are controlled mainly by pressure and temperature, as well as the composition of the metallic phase, and oxygen fugacity (Bouhifd & Jephcoat, 2003, 2011, Siebert et al., 2012, Fischer et al., 2015). To obtain partitioning behavior independent of oxygen fugacity, we use the exchange partition coefficient K_d, which is the thermodynamical constant of the reaction:

$$MO_{n/2} + \frac{n}{2} Fe \rightarrow \frac{n}{2} FeO + M \qquad (13)$$

Where M is the element considered (in our case Ni or Co), and n is the valence of the element M (in our case, n= 2). In reaction (13), the oxides are in the silicate phase, while the reduced element is in the metallic phase. The exchange partition coefficient is given by $K_d = \frac{c_M}{c_{MO_{n/2}}} \times \left(\frac{c_{FeO}}{c_{Fe}}\right)^{n/2}$ where c_M and c_{Fe} are the molar fractions of M and Fe in the metallic phase, and c_{FeO} and $c_{MO_{n/2}}$ are the molar fractions of FeO and $MO_{n/2}$ in the silicate phase. To estimate the values of the partition coefficients, we use the parameterization of K_d from Clesi et al., (2016), where we ignore the effect of water, as well as the carbon content in the metallic phase. The exchange partition coefficient, K_d, is given by:

$$logK_d^{element} = \frac{b_{el}}{T} + c_{el}\frac{P}{T} + e_{el}log\left(1 - \chi_{Si}^{metal}\right) + g_{el}log\left(1 - \chi_S^{metal}\right) + h_{el} \quad (14)$$

The parameters b_{el}, c_{el}, e_{el}, g_{el} and h_{el} are detailed in Clesi et al., (2016), and are different for each element studied. *P* and *T* are the pressure (in GPa) and temperature (in Kelvin) of equilibrium, respectively, corresponding to the pressure at 50% of CMB depth (i.e., 1450 km), and the liquidus temperature associated with it (Andrault et al., 2011). We assume here an equilibrium pressure of 63 GPa, and an equilibrium temperature of 3450 K. χ_{Si}^{metal} and χ_S^{metal} are the mass fractions of silicon and sulfur in the impactor. We assume here that χ_{Si}^{metal} =0.06 and χ_S^{metal} =0.019 (McDonough, 2003). K_d is then converted into a Nernst partition coefficient (mass ratio) following:

$$D^{met/sil} = \frac{M_{oxide} \times M_{Fe}}{M_{FeO} \times M_{element}} \times K_d^{element} \times D_{Fe}^{met/sil} \quad (15)$$

where $M_{element}$ is the molar mass of Ni or Co, M_{oxide} is the molar mass of NiO or CoO, and M_{Fe} and M_{FeO} are the molar masses of Fe and FeO respectively. $D_{Fe}^{met/sil}$ is the partition coefficient of iron and equals 13.65 in the BSE model. We consider that the impactor does not significantly change the oxygen fugacity and therefore does not influence the $D_{Fe}^{met/sil}$ value.

909 The second term in Eq. (11) characterizes the influence of the Reynolds number, which is
910 given by Eq. (6). As stated in Section 4, we consider that the metal fragments into droplets
911 with a radius of 1 cm. The sinking velocity of these droplets is given by Eq. (9). We
912 assume here a silicate density of ρ_{mantle} =4500 kg.m^{-3} (mean density of the Earth's mantle),
913 a metallic density of ρ_{metal}= 9400 kg.m^{-3}, which is consistent with iron rich liquid alloys
914 at these pressures (Morard et al., 2013) and the current Earth's value for the acceleration
915 of gravity (i.e., 9.81 m.s^{-2}). The viscosity of the silicate phase in our calculations ranges
916 from 0.1 to 100 Pa.s. The third term in Eq. (11) measures the influence of the viscosity
917 ratio $R_\mu = \mu_{met}/\mu_{sil}$. In our calculations, we consider a constant value for the metallic
918 viscosity (= 0.1 Pa.s), consistent with iron liquid viscosity at high pressure (Kono et al.,
919 2015).
920
921 Once the parameter *Rc* is calculated for Ni and Co, the impactor equilibrates with a volume
922 of mantle defined by Eq. (12) in section 4, considering that $V_{impactor}/V_{affected}$ = 0.0016,
923 independent of the size of the impactor. As R_C expresses the volume fraction of the silicate
924 that has reacted with the metal, it may overestimate the volume of the mantle that has
925 equilibrated with the metal phase. Hence the parameter R_C should be considered as a first-
926 order approximation of the volume equilibrated. Therefore, for Eq. (12), the mass of
927 mantle that is equilibrated is obtained by simple multiplication by ρ_{mantle}. In this mass of

928 mantle, the concentration of Ni or Co is in equilibrium and is given by $\chi_{eq}^{silicate} =$

929 $\frac{\chi_{impactor}^{metal}}{D^{met/sil}}$. The final mass fraction of Ni or Co is given by:

930

931 $$\chi_{final}^{silicate} = \chi_{initial}^{silicate} + (\chi_{eq}^{silicate} - \chi_{initial}^{silicate}) \frac{m_{equilibrated}}{m_{mantle}} \quad (16)$$

932

933 where, $\chi_{final}^{silicate}$ is the concentration of Ni or Co in the final mantle, $\chi_{initial}^{silicate}$ is the initial

934 concentration of Ni or Co in the mantle, $\chi_{eq}^{silicate}$ is the concentration at equilibrium,

935 $m_{equilibrated}$ is the mass that is equilibrated and m_{mantle} is the mass of the Earth's mantle. The

936 final Ni/Co ratio is then derived from $\chi_{final}^{silicate}$ for Ni and Co. The results of calculations

937 for different viscosities as a function of the impactor radius are presented in Fig. 16.

938

939

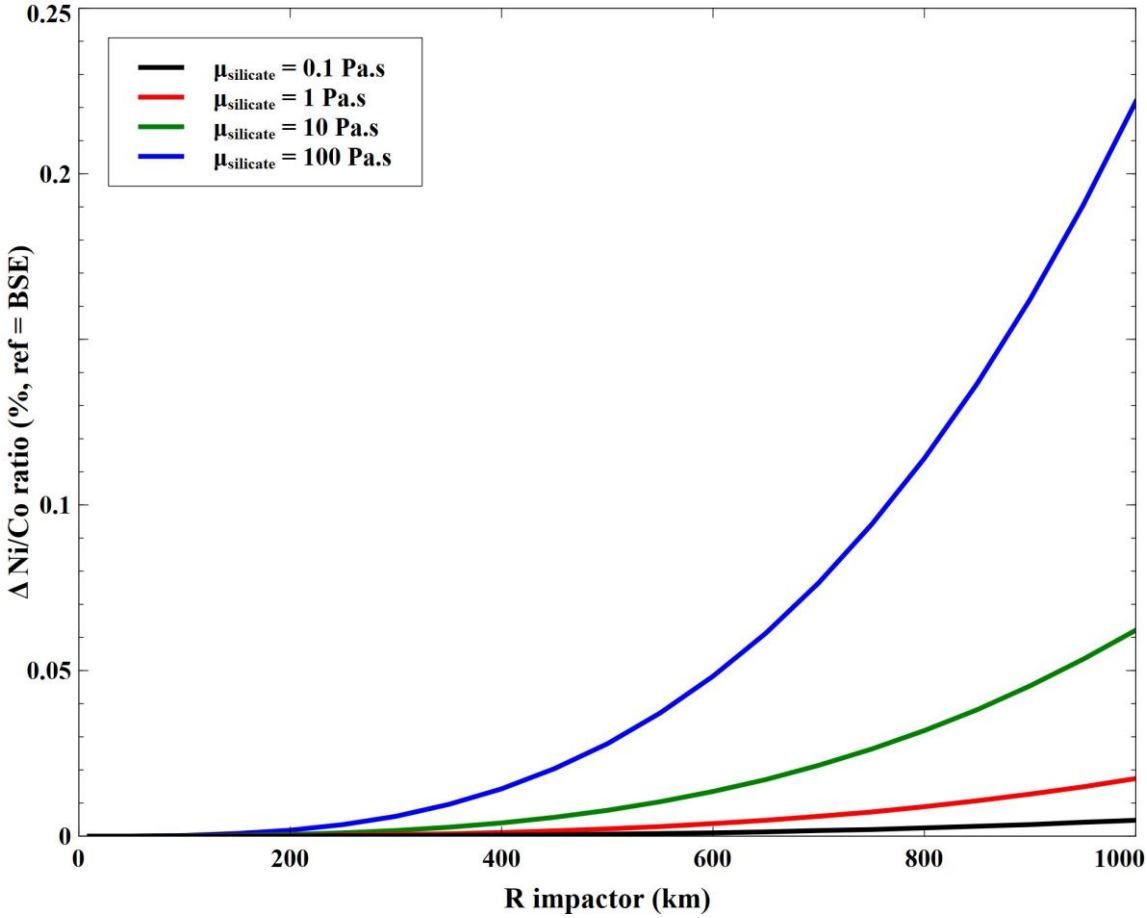

Figure 16: Evolution of Ni/Co ratio in the mantle after an impact as a function of the impactor size for different silicate viscosities (0.1 to 100 Pa.s). We represent here the variation of the Ni/Co ratio after the impact relative to the initial BSE concentration: $\Delta\left(\frac{Ni}{Co}\right) = 100 \times \frac{\left(\frac{Ni}{Co}\right)_{Final} - \left(\frac{Ni}{Co}\right)_{BSE}}{\left(\frac{Ni}{Co}\right)_{BSE}}$. Since the impact happens on the BSE, the more the Ni/Co ratio is different to that of the BSE, the more the impactor has reached equilibrium.

947

948 Fig. 16 shows that a single impactor, even a large one, does not significantly affect the
949 Ni/Co ratio in the mantle. The maximum variation is 0.25 %, and is obtained for a large
950 impactor (1000 km radius) for a relatively high viscosity of the magma ocean (100 Pa.s).
951 For low viscosities (0.1 and 1 Pa.s), a metallic impactor weakly affects the Ni/Co ratio in
952 the mantle (less than 0.1 % change for a 1000 km radius impactor). Such a small variation
953 confirms that high spatial resolution models are not necessary even for large Pe_{mesh} values
954 obtained for low viscosities. For a relative error of 100% in the values of R_c , at a viscosity
955 of 0.1 Pa.s, it would only induce a variation in Ni/Co of between 0 and 0.2% within the
956 final model.
957 Eq. (16) shows that the final concentration is proportional to the volume equilibrated if
958 $\chi_{eq}^{silicate}$ is higher than $\chi_{initial}^{silicate}$. In this case, late accretion of a metallic impactor, which
959 yields a high metallic concentration in Ni and Co (similar to the Earth core concentration
960 given in McDonough, 2003); with a high equilibrium pressure, which yields low partition
961 coefficient values for Ni and Co, $(\chi_{eq}^{silicate} - \chi_{initial}^{silicate})$ is positive. The impactor is
962 metallic and rich in Ni and Co (5.2%wt and 0.24 %wt, respectively), and impacts a silicate
963 mantle with a BSE composition. Therefore, when the mass of mantle equilibrated is
964 higher, the variation in Ni or Co concentration compared to the BSE in the mantle is
965 higher. If the disequilibrium is high, the $m_{equilibrated}$ is low, and therefore there is less
966 variation in the Ni/Co ratio. As shown in Fig. 16, the amount of disequilibrium is higher

967 for a low viscosity magma ocean, as well as for small metallic impactors, and therefore
968 there is no change in the moderately siderophile element concentrations in the mantle
969 under these conditions. This means that, to have a significant effect on the moderately
970 siderophile element concentrations in the BSE, late accretion impactors need to be large
971 and impact a viscous magma ocean in order to increase the degree of equilibrium. Even
972 in this case, if the amount of Ni and Co in the impactor is not significantly higher than that
973 in the Earth's core, the change in BSE composition will not be significant, as illustrated
974 in Fig. 16.
975

976 ## 6. Discussion

977 ### 6.1. Earth accretion models and magma ocean properties

978 In the previous section we characterized the effects of a late impact, negligible in mass,
979 composed only of a metallic phase. However, most of the disequilibrium happens during
980 accretion. Therefore, Eq. (16) is not relevant, at least not in this form, in the context of a
981 growing planet. Assuming that the mantle of the impactor and of the growing Earth is well
982 mixed before equilibration with the metallic fraction, we can define the concentration of
983 the post-impact mantle, $\chi^{silicate}_{post-impact}$. By modifying Eq. (16), and knowing the
984 composition of the impactor's metallic phase it is possible to calculate the composition of

985 a growing planetary mantle before it equilibrates with the metallic phase of the impactor.
986 It is given by:

987 $$\chi^{silicate}_{post-impact} = \frac{m_{mantle}}{m_{mantle}-m_{equilibrated}}\left(\chi^{silicate}_{final} - \frac{m_{equilibrated}}{m_{mantle}}\chi^{silicate}_{equilbrated}\right) (17)$$

988 Since $m_{equilibrated}$ is dependent on the size of the impactor core and magma ocean viscosity,
989 it is possible to calculate the composition of the mantle for a 90% accreted Earth hit by a
990 Mars-sized impactor (Moon-forming impact) as a function of the impactor's core radius
991 and viscosity of the magma ocean. Fig. 17 shows the corresponding results for comparison
992 with Fig. 16: in this case, the greater the degree of equilibrium, the lower the initial Ni/Co
993 ratio.
994

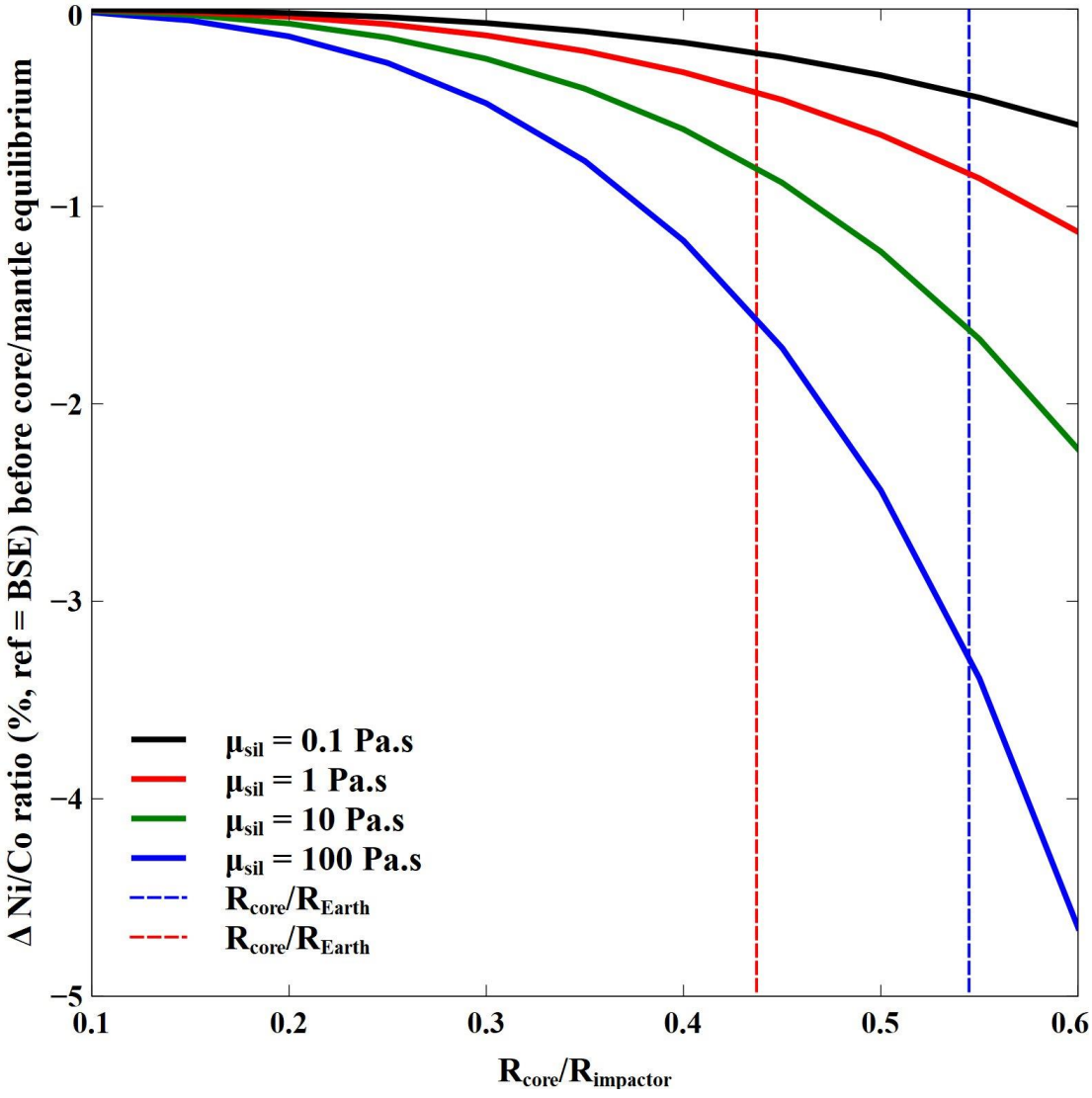

995

996 **Figure 17:** Ni/Co ratio in the Earth's mantle before equilibration with the core of an
997 impactor corresponding to 10% of the Earth's mass as a function of the radius of the
998 impactor's core normalized to the impactor size and for different magma ocean viscosities.
999 The R_{core}/R_{Earth} current ratio is shown by the blue dashed line, and the R_{core}/R_{Mars} ratio by
1000 a red dashed line. In the calculation, the impactor is the same size as Mars ($R_{impactor}$ = 3390
1001 km), and the impactor core radius ranges from 340 km to 2040 km. We represent here the
1002 variation in Ni/Co ratio before the impact relative to the BSE concentration but for a well-
1003 mixed mantle after impact: $\Delta\left(\frac{Ni}{Co}\right) = 100 \times \frac{(\frac{Ni}{Co})_{post-impact} - (\frac{Ni}{Co})_{BSE}}{(\frac{Ni}{Co})_{BSE}}$.

1004

1005 The results displayed in Fig. 17 show that it is possible to reach the same final Ni/Co ratio
1006 for the Earth's mantle with drastically different properties of the impactor and the magma
1007 ocean. From Fig. 17, two post-impact models can be derived:

1008 - A model with a low $R_{core}/R_{impactor}$ ratio and low magma ocean viscosity,
1009 which yields a lower degree of equilibrium between metal and silicate. In this kind
1010 of model, the composition of the Earth's mantle is more dependent on the
1011 equilibrium conditions between the metallic phase and the silicate phase than on
1012 the composition of the impactor. For instance, the models presented in *e.g.* Burbine
1013 & O'Brien (2004), Rai & van Westrenen (2013) or Dauphas et al., (2014) are based
1014 on mixing different chondritic compositions where the main parameter fitted is the
1015 isotopic consistency, and they are therefore predominantly compositionally-
1016 derived models. For these models to be consistent, the impactor's core needs to be
1017 small ($R_{core}/R_{impactor}$ < 0.4, left-hand side of Fig. 17), and the magma ocean
1018 viscosity low ($\mu_{magma\ ocean} \approx$ 0.1- 1 Pa.s), so as to achieve a low equilibrium rate
1019 between metal and silicate.

1020 - A model with a high $R_{core}/R_{impactor}$ ratio, and high viscosity of the magma
1021 ocean, which yields greater equilibrium between metal and silicate. In this kind of
1022 model, the main changes in Earth mantle composition are due more to the
1023 composition of the impactor and less to the chemical reactions between metal and

1024 silicate. For instance, the models presented in *e.g.* Wood et al., 2008, Siebert et al.,
1025 2012 and Boujibar et al., 2014 are based on the metal-silicate partitioning behavior,
1026 where the discriminating parameter is the relative core/mantle abundances of
1027 siderophile elements, and they are therefore predominantly equilibrium-derived
1028 models. In this kind of model, a minimal equilibrium needs to be reached, and
1029 therefore the impactor's core needs to be large ($R_{core}/R_{impactor} > 0.4$, right-hand side
1030 of Fig. 17), and/or the magma ocean viscosity needs to be high ($\mu_{magma\ ocean} \approx$ 10-
1031 100 Pa.s).

1032 To summarize, our results cannot constrain the viscosity of the magma ocean (especially
1033 given the error in our calculations for low viscosity calculations, see Section 2.4), but for
1034 a given model, our results can constrain the range of magma ocean viscosities in order to
1035 reach the BSE concentrations for moderately siderophile elements.

1036 However, this work needs to be done for each accretion step or impact, and for each
1037 element, which would increase the number of plausible scenarios to accrete the Earth, but
1038 could also provide compositional constraints on irreconcilable scenarios, and therefore
1039 allow some impactor compositions to be excluded from a given model.

1040

1041 ### 6.2. Effect of Moon formation on the Ni/Co ratio in the Earth's mantle

1042 In the previous section we showed that the properties of the magma ocean are model
1043 dependent: they have to be inferred from the impactor properties and the final BSE content

chosen as a control of the model output. In this section, we infer the viscosity of a magma ocean for one particular model: the Moon formation by an impact with a Mars-sized impactor (Canup, 2004). The Moon forming impactor (named Theia) is believed to be a large Mars-sized impactor which hit the proto-Earth at the end of accretion with an oblique trajectory (Canup & Asphaug, 2001, Canup, 2004). In a simulation of this kind of impact, most of the metal and silicate of the impactor merges with the Earth (Canup, 2004). If we consider mass of the Moon to be negligible compared to that of Theia, and ignore the loss of particles due to the impact, we can determine that the final 10% mass accreted to the Earth was due to the impact with Theia. The core of this impactor is 30% of the total mass of the impactor (Canup, 2004), with the same mean density as the Earth, so it is not improbable that the ratio $R_{core}/R_{impactor}$ is comparable to that of the Earth or Mars today (given by the red and blue vertical lines in Figs. 17). In that case, Eq. (17) and Fig. 17 shows that some equilibrium occurred between the magma ocean formed by the impact and the impactor's core sinking into the Earth's core. For every magma ocean viscosity tested here, it is necessary to have interaction between Theia's core and the proto-Earth's mantle to get the final BSE concentration. For a magma ocean viscosity of 0.1 Pa.s, the proto-Earth's Ni/Co ratio is between 0.25 % and 0.45 % lower than the BSE values for a $R_{core}/R_{impactor}$ comparable to those of Mars and the Earth respectively. For a magma ocean viscosity of 100 Pa.s, the proto-Earth Ni/Co ratio is between 1.45% and 3.00 % lower than the BSE values for a $R_{core}/R_{impactor}$ comparable to those of Mars and the Earth, respectively.

1064 This means that the Moon forming impact had a significant effect on the BSE Ni/Co ratio,
1065 which can be high if the magma ocean formed after the impact was viscous (100 Pa.s) and
1066 the core radius of Theia was around 1850 km.
1067
1068
1069 ## 7. Conclusion

1070 We developed numerical models to characterize the effects of viscosity and partition
1071 coefficients on the metal/silicate equilibrium for moderately siderophile elements. We
1072 showed that the volume of silicate equilibrated with a small volume of metal is mostly
1073 controlled by the partition coefficients and the viscosity of the silicate. The viscosity ratio
1074 between metal and silicate is a second order parameter but still has a significant effect.
1075 The scope of this study does not include other elements that have different partitioning
1076 behavior (V, Cr, Mn etc.) and future models of equilibrium between metal and silicate
1077 will have to integrate these elements to get a clearer view of chemical exchanges within
1078 the Early Earth. Furthermore, the range of *Re* and *We* covered in this study does not cover
1079 the whole range of *Re* and *We* numbers during the accretion event (Fig. 10). Therefore, in
1080 the future, we will need to model more complex flows (such as shown in Samuel, 2012 or
1081 Wacheul et al., 2014), to widen the scope of our interpretations (see Section 4 for the
1082 extrapolation conditions). Future models should also account for the thermal equilibration
1083 during metal/silicate separation (Wacheul & Le Bars, 2018) to characterize the effects of

temperature on the partition coefficient values. Other phenomena, while important, are ignored due to being beyond the scope of the study, for instance the effect of the droplet size and shape (Qaddah et al., 2019), or stretch-enhancing diffusion (Lherm & Deguen, 2018), or the possibility of large core-merging events (Landeau et al., 2016). All these phenomena are beyond the scope of this study and should be taken into account in further work and models of accretion.

Nevertheless, we proposed a parameterization of the disequilibrium between a silicate magma ocean and a metallic droplet for moderately siderophile element behavior. Using this parameterization on Ni and Co behavior at the end of accretion, it is possible to define some constraints on the viscosity of the magma ocean. For a given model of accretion to fit the current BSE concentrations, the viscosity of the magma ocean and the impactor composition need to be changed accordingly: large impactors with large metallic cores (R_{core} > 1100 km) and high magma ocean viscosity (10 -100 Pa.s) favor a high degree of metal/silicate equilibrium; while metal/silicate disequilibrium models can be achieved with moderately small metallic cores (R_{core} ≈ 300-1000 km) and low viscosity (0.1 - 1 Pa.s) magma ocean.

When applying our results to the Moon-forming impact, we showed that the current Ni/Co ratio in the BSE is affected by the Moon's formation, depending on the viscosity of the magma ocean formed after the impact. The Moon's formation can account for 0.25 to 0.45

1103 % of the final BSE Ni/Co ratio for a low viscosity (0.1 Pa.s) magma ocean, and for 1.45%
1104 to 3 % of the final BSE Ni/Co ratio for a high viscosity (100 Pa.s) magma ocean.
1105

Acknowledgments

This research received funding from the French PNP program (INSU-CNRS), the French Government Laboratory of Excellence initiative No. ANR-10-LABX- 0006 and the Région Auvergne. This paper is Laboratory of Excellence ClerVolc contribution No. **421**. This project has received funding from the European Research Council (ERC) under the European Union's Horizon 2020 research and innovation programme (grant agreement 681835 FLUDYCO-ERC-2015-CoG). This project has received funding from the European Research Council (ERC) under the European Union's Horizon 2020 research and innovation programme (grant agreement 716429). We thank Renaud Deguen for his fruitful comments.

References

C. J. Allegre, J.-P. Poirier, E. Humler, and A. W. Hofmann. The Chemical composition of the Earth. *Earth and Planetary Science Letters*, 134:515–526, 1995.

D. Andrault, N. Bolfan-Casanova, G. Lo Nigro, M. A. Bouhifd, G. Garbarino and M. Mezouar. Solidus and liquidus profiles of chondritic mantle: Implication for melting of

the Earth across its history. *Earth and planetary science letters*, 304(1-2):251-259, 2011.

M. A. Bouhifd and A.P. Jephcoat. Convergence of Ni and Co metal-silicate partition coefficients in the deep magma-ocean and coupled silicon-oxygen solubility in iron melts at high pressures. *Earth and Planetary Science Letters*, 307(3-4):341–348, 2011.

M. A. Bouhifd and A.P Jephcoat. The effect of pressure on partitioning of Ni and Co between silicate and iron-rich metal liquids: a diamond-anvil cell study. *Earth and Planetary Science Letters*, 209(1-2):245–255, 2003.

M.A. Bouhifd, V. Clesi, A. Boujibar, N. Bolfan-Casanova, C. Cartier, T. Hammouda, M. Boyet, G. Manthilake, J. Monteux and D. Andrault. Silicate melts during Earth's core formation. *Chemical Geology*, 461, 128-139, 2017.

A. Boujibar, D. Andrault, M. A. Bouhifd, N. Bolfan-Casanova, J.-L. Devidal, and N. Trcera. Metal-silicate partitioning of sulphur, new experimental and thermodynamic constraints on planetary accretion. *Earth and Planetary Science Letters*, 391:42– 54, 2014.

1144 T.H. Burbine, and K.M. O'Brien. Determining the possible building blocks of the Earth
1145 and Mars. *Meteoritics & Planetary Science*, 39(5):667-681, 2004.
1146
1147 C. Cartier, T. Hammouda, M. Boyet, M. A. Bouhifd and J.-L. Devidal. Redox control
1148 of the fractionation of niobium and tantalum during planetary accretion and core
1149 formation. *Nature Geoscience*, 7(8):573, 2014
1150
1151 R.M. Canup. Simulations of a late lunar-forming impact. *Icarus*, 168(2):433–456,
1152 2004.
1153
1154 R. M. Canup. Accretion of the Earth. *Philosophical Transactions of the Royal Society*
1155 *A: Mathematical, Physical and Engineering Sciences*, 366(1883):4061-4075, 2008.
1156
1157 R. M. Canup, and E. Asphaug. Origin of the Moon in a giant impact near the end of the
1158 Earth's formation. *Nature*, 412(6848):708, 2001.
1159
1160 I. D. Chang.On the wall effect correction of the Stokes drag formula for axially
1161 symmetric bodies moving inside a cylindrical tube. *Zeitschrift für angewandte*
1162 *Mathematik und Physik ZAMP*, 12(1):6-14, 1961.

V. Clesi, M.A. Bouhifd, N. Bolfan-Casanova, G. Manthilake, A. Fabbrizio, and D. Andrault. Effect of H2O on metal-silicate partitioning of Ni, Co, V, Cr, Mn and Fe: Implications for the oxidation state of the Earth and Mars. *Geochimica et Cosmochimica Acta*, 192:97–121, 2016.

J. Crank. *The Mathematics of Diffusion*, 2nd ed. Clarendon Press, Oxford. viii, 414 p, 1975.

T. W. Dahl and D. J. Stevenson. Turbulent mixing of metal and silicate during planet accretion and interpretation of the Hf-W chronometer. *Earth and Planetary Science Letters*, 295(1-2):177–186, 2010.

N. Dauphas, J. H. Chen, J. Zhang, D. A. Papanastassiou, A. M. Davis, and C. Travaglio. Calcium-48 isotopic anomalies in bulk chondrites and achondrites: Evidence for a uniform isotopic reservoir in the inner protoplanetary disk. *Earth and Planetary Science Letters*, 407:96-108, 2014.

R. Deguen, P.Olson, and P. Cardin. Experiments on turbulent metal-silicate mixing in a magma ocean. *Earth and Planetary Science Letters*, 310(3-4):303–313, 2011

R. Deguen, M. Landeau, and P.Olson. Turbulent metal-silicate mixing, fragmentation, and equilibration in magma oceans. *Earth and Planetary Science Letters*, 391:274–287, 2014.

M. J. Drake, and K. Righter. Determining the composition of the Earth. *Nature*, 416(6876):39, 2002.

R. A. Fischer, Y. Nakajima, A. J. Campbell, D. J. Frost, D. Harries, F. Langenhorst, N. Miyajima, K. Pollok, and D. C. Rubie. High pressure metal-silicate partitioning of Ni, Co, V, Cr, Si, and O. *Geochimica et Cosmochimica Acta*, 167:177–194, 2015.

J. R. Fleck, C. L. Rains, D. S. Weeraratne, C. T. Nguyen, D. M. Brand, S. M Klein, J. M. McGehee, J. M. Rincon, C. Martinez and P.L Olson. Iron diapirs entrain silicates to the core and initiate thermochemical plumes. *Nature communications*, *9*(1), 71, 2018.

B. Jacobsen, Q.- Z. Yin, F. Moynier, Y.Amelin, A. N. Krot, K. Nagashima, I. D. Hutcheon, and H. Palme. 26Al-26Mg and 207Pb-206Pb systematics of Allende CAIs: Canonical solar initial 26Al/27Al ratio reinstated. *Earth and Planetary Science Letters*, 272(1-2):353–364, 2008.

1203 J. H. Jones and M. J. Drake. Geochemical constraints on core formation in the Earth.
1204 *Nature*, 322(6076):221, 1986.
1205
1206 B. B., Karki, D. B., Ghosh, and S. K. Bajgain. Simulation of Silicate Melts Under
1207 Pressure. In *Magmas Under Pressure* : 419-453, 2018
1208
1209 B; B. Karki. and L. P. Stixrude. Viscosity of MgSiO3 liquid at Earth's mantle
1210 conditions: Implications for an early magma ocean. *Science*, 328(5979):740-742, 2010.
1211
1212 Y. Ke and Solomatov, V. S. Coupled core-mantle thermal evolution of early Mars.
1213 *Journal of Geophysical Research: Planets*, 114(E7), 2009
1214
1215 J. D. Kendall and H. J. Melosh. Differentiated planetesimal impacts into a terrestrial
1216 magma ocean: fate of the iron core. *Earth and Planetary Science Letters*, 448:24–33,
1217 2016.
1218
1219 T. Kleine, C. Munker, K. Mezger, and H. Palme. Rapid accretion and early core
1220 formation on asteroids and the terrestrial planets from Hf-W chronometry. *Nature*,
1221 418(6901):952–955, 2002.
1222

T. Kleine, M. Touboul, B. Bourdon, F. Nimmo, K. Mezger, H. Palme, S.B. Jacobsen, Q.-Z. Yin, and A.N. Halliday. Hf–W chronology of the accretion and early evolution of asteroids and terrestrial planets. *Geochimica et Cosmochimica Acta*, 73(17):5150–5188, 2009.

T. Kleine and J. F. Rudge. Chronometry of meteorites and the formation of the Earth and Moon. *Elements*, 7(1):41–46, 2011.

Y. Kono, C. Kenney-Benson, Y. Shibazaki, C. Park, G. Shen, and Y.Wang. High-pressure viscosity of liquid Fe and FeS revisited by falling sphere viscometry using ultrafast X-ray imaging. *Physics of the Earth and Planetary Interiors*, 241:57–64, 2015.

M. Landeau, P. Olson, R. Deguen and B. H. Hirsh. Core merging and stratification following giant impact. *Nature Geoscience*, 9(10):786, 2016.

V. Lherm and R. Deguen. Small-Scale Metal/Silicate Equilibration During Core Formation: The Influence of Stretching Enhanced Diffusion on Mixing. *Journal of Geophysical Research: Solid Earth*, 123(12):10,496-10,516, 2018.

C. Liebske, B. Schmickler, H. Terasaki, B. T. Poe, A. Suzuki, K. I. Funakoshi, K.i. Funakochi, R. Ando and D. C. Rubie. Viscosity of peridotite liquid up to 13 GPa: Implications for magma ocean viscosities. *Earth and Planetary Science Letters*, 240(3-4):589-604, 2005.

U. Mann, D. J. Frost and D. C. Rubie. Evidence for high-pressure core-mantle differentiation from the metal–silicate partitioning of lithophile and weakly-siderophile elements. *Geochimica et Cosmochimica Acta*, 73(24):7360-7386, 2009.

W. F. McDonough. 3.16–Compositional model for the Earth's core. *Treatise on geochemistry*, :547-568, 2003.

W. F. McDonough and S.-S. Sun. The composition of the Earth. *Chemical Geology*, (120): 223–253, 1995.

R. C. Mittal and R. K. Jain. Redefined cubic B-splines collocation method for solving convection–diffusion equations. *Applied Mathematical Modelling*, 36(11)): 5555-5573, 2012.

J. Monteux, Y. Ricard, N. Coltice, F. Dubuffet and M. Ulvrova. A model of metal–silicate separation on growing planets. *Earth and Planetary Science Letters*, *287*(3-4):353-362, 2009.

J. Monteux, H. Amit, G. Choblet, B. Langlais and G. Tobie. Giant impacts, heterogeneous mantle heating and a past hemispheric dynamo on Mars. *Physics of the Earth and Planetary Interiors*, 240:114-124, 2015.

G. Morard, J. Siebert, D. Andrault, N. Guignot, G. Garbarino, F. Guyot, F. and D. Antonangeli. The Earth's core composition from high pressure density measurements of liquid iron alloys. *Earth and Planetary Science Letters*, 373:169-178, 2013.

M. Nakajima and D. J. Stevenson. Melting and mixing states of the Earth's mantle after the Moon-forming impact. *Earth and Planetary Science Letters*, 427:286-295, 2015

D. P. O'Brien, A. Morbidelli and H.F. Levison. Terrestrial planet formation with strong dynamical friction. *Icarus*, 184(1):39-58, 2006.

E. Olsson, and G. Kreiss. A conservative level set method for two phase flow. *Journal of computational physics*, 210(1):225-246, 2005.

B. Qaddah, J. Monteux, V. Clesi, M. A. Bouhifd and M. Le Bars. Dynamics and stability of an iron drop falling in a magma ocean. *Physics of the Earth and Planetary Interiors*, 289:75-89, 2019.

B. Qaddah , J. Monteux and M. Le Bars. Thermal evolution of a metal drop falling in a less dense, more viscous fluid. Physical Review Fluids, Accepted manuscript April 2020

N. Rai, and W. van Westrenen. Core-mantle differentiation in Mars. *Journal of Geophysical Research: Planets*, 118(6):1195-1203, 2013.

Y. Ricard, O. Šrámek, and F. Dubuffet. A multi-phase model of runaway core-mantle's segregation in planetary embryos. *Earth and Planetary Science Letters*, 284(1-2):144–150, 2009.

K. Righter. Prediction of metal-silicate partition coefficients for siderophile elements: An update and assessment of P-T conditions for metal-silicate equilibrium during accretion of the Earth. *Earth and Planetary Science Letters*, 304(1-2):158–167, 2011.

D. C. Rubie, D.J. Frost, U. Mann, Y. Asahara, F. Nimmo, K. Tsuno, P. Kegler, A. Holzheid, and H. Palme. Heterogeneous accretion, composition and core-mantle differentiation of the Earth. *Earth and Planetary Science Letters*, 301(1-2):31–42, 2011.

D.C. Rubie, H.J. Melosh, J.E. Reid, C. Liebske, and K. Righter. Mechanisms of metal-silicate equilibration in the terrestrial magma ocean. *Earth and Planetary Science Letters*, 205(3-4): 239–255, 2003.

D.C. Rubie, S.A. Jacobson, A. Morbidelli, D.P. O'Brien, E.D. Young, J. de Vries, F. Nimmo, H. Palme, and D.J. Frost. Accretion and differentiation of the terrestrial planets with implications for the compositions of early-formed Solar System bodies and accretion of water. *Icarus*, 248:89–108, 2015.

J. F. Rudge, T. Kleine, and B. Bourdon. Broad bounds on Earth's accretion and core formation constrained by geochemical models. *Nature Geoscience*, 3(6):439–443, 2010.

H. Samuel and P. J. Tackley. Dynamics of core formation and equilibration by negative diapirism. *Geochemistry, Geophysics, Geosystems*, 9(6), 2008.

H. Samuel. A re-evaluation of metal diapir breakup and equilibration in terrestrial magma oceans. *Earth and Planetary Science Letters*, 313-314:105–114, 2012.

E. M. Shoemaker. Interpretation of lunar craters. *Physics and Astronomy of the Moon* : 283-359, 1962

J. Siebert, J. Badro, D. Antonangeli, and F. J. Ryerson. Metal-silicate partitioning of Ni and Co in a deep magma ocean. *Earth and Planetary Science Letters*, 321-322:189–197, 2012.

D.J. Stevenson. Models of the Earth's core. *Science*, 214(4521):611–619, 1981.

M. Ulvrová, N. Coltice, Y. Ricard, S. Labrosse, F. Dubuffet, J. Velímský, and O. Šrámek. Compositional and thermal equilibration of particles, drops, and diapirs in geophysical flows. *Geochemistry, Geophysics, Geosystems*, 12(10), 2011.

O. Šrámek., Y. Ricard, and F. Dubuffet. A multiphase model of core formation. *Geophysical Journal International*, 181(1):198–220, 2010.

J.-B. Wacheul and M. Le Bars. Fall and fragmentation of liquid metal in a viscous fluid. *Physical Review Fluids*, 2(9):090507, 2017.

J.-B. Wacheul and M. Le Bars. Experiments on fragmentation and thermo-chemical exchanges during planetary core formation. *Physics of the Earth and Planetary Interiors*, 276:134-144, 2018.

J-B-Wacheul, M. Le Bars, J. Monteux, and J. M. Aurnou. Laboratory experiments on the breakup of liquid metal diapirs. *Earth and Planetary Science Letters*, 403: 236–245, 2014.

K.J. Walsh, A. Morbidelli, S.N. Raymond, D.P. O'Brien, and A.M. Mandell. A low mass for mars from Jupiter's early gas-driven migration. *Nature*, 475(7355):206–209, 2011.

G. W. Wetherill. Occurrence of giant impacts during the growth of the terrestrial planets. *Science*, 228(4701):877-879, 1985.

J. Wade and B. J. Wood. Core formation and the oxidation state of the Earth. *Earth and Planetary Science Letters*, 236(1-2):78-95, 2005.

B. J. Wood, M. J. Walter, and J. Wade. Accretion of the Earth and segregation of its core. *Nature*, 441(7095):825–833, 2006.

B. J. Wood, J. Wade, and M. R. Kilburn. Core formation and the oxidation state of the Earth: Additional constraints from Nb, V and Cr partitioning. *Geochimica et Cosmochimica Acta*, 72(5):1415–1426, 2008.